AIP | Physics of Fluids

Turbulence- and buoyancy-driven secondary flow in a horizontal square duct heated from below

A. Sekimoto, G. Kawahara, K. Sekiyama, M. Uhlmann, and A. Pinelli

Citation: Phys. Fluids **23**, 075103 (2011); doi: 10.1063/1.3593462
View online: http://dx.doi.org/10.1063/1.3593462
View Table of Contents: http://pof.aip.org/resource/1/PHFLE6/v23/i7
Published by the AIP Publishing LLC.

Turbulence- and buoyancy-driven secondary flow in a horizontal square duct heated from below

A. Sekimoto,[1] G. Kawahara,[1,a)] K. Sekiyama,[1] M. Uhlmann,[2] and A. Pinelli[3]
[1]*Department of Mechanical Science, Osaka University, 560-8531 Osaka, Japan*
[2]*Institute for Hydromechanics, Karlsruhe Institute of Technology, 76128 Karlsruhe, Germany*
[3]*Modeling and Numerical Simulation Unit, CIEMAT, 28040 Madrid, Spain*

(Received 14 July 2010; accepted 5 April 2011; published online 12 July 2011)

Direct numerical simulations of fully developed turbulent flows in a horizontal square duct heated from below are performed at bulk Reynolds numbers $Re_b = 3000$ and 4400 (based on duct width H) and bulk Richardson numbers $0 \leq Ri \leq 1.03$. The primary objective of the numerical simulations concerns the characterization of the mean secondary flow that develops in this class of flows. On one hand, it is known that turbulent isothermal flow in a square duct presents secondary mean motions of Prandtl's second kind that finds its origin in the behavior of turbulence structures. On the other hand, thermal convection drives a mean secondary motion of Prandtl's first kind directly induced by buoyancy. As far as the mean structure of the cross-stream motion is concerned, it is found that different types of secondary flow regimes take place when increasing the value of the Richardson number. The mean secondary flow in the range $0.025 \lesssim Ri \lesssim 0.25$ is characterized by a single large-scale thermal convection roll and four turbulence-driven corner vortices of the opposite sense of rotation to the roll, as contrasted with the classical scenario of the eight-vortex secondary flow pattern typical of isothermal turbulent square-duct flow. This remarkable structural difference in the corner regions can be interpreted in terms of combined effects, on instantaneous streamwise vortices, of the large-scale circulation and of the geometrical constraint by the duct corner. When further increasing the Richardson number, i.e., $Ri \gtrsim 0.25$, the structure of the mean secondary flow is solely determined by the large-scale circulation induced by the buoyancy force. In this regime, the additional mean cross-stream motion is characterized by the presence of two distinct buoyancy-driven vortices of opposite sense of rotation to the circulation only in two of the four corner regions. With increasing Ri, the large-scale circulation is found to enhance the wall skin friction and heat transfer. In the significant-buoyancy regime $Ri \gtrsim 0.25$, the mean cross-stream motion and its rms fluctuations are found to scale, respectively, with the buoyancy-induced velocity $u_g = \sqrt{g\beta\Delta T H}$ (g, β, and ΔT being the gravity acceleration, the volumetric coefficient of thermal expansion, and the temperature difference across the duct, respectively) and with the mixed velocity scale $\sqrt{(\nu/H)u_g}$ (ν being the kinematic viscosity). It is suggested that the probable scalings for the rms of streamwise velocity component and of temperature fluctuation are related with the friction velocity u_τ and friction temperature T_τ according to the magnitudes $u_\tau^2/\sqrt{(\nu/H)u_g}$ and $T_\tau u_\tau/\sqrt{(\nu/H)u_g}$, respectively. © *2011 American Institute of Physics*. [doi:10.1063/1.3593462]

I. INTRODUCTION

The existence of secondary flow of Prandtl's second kind (referred to as SFP2nd in this paper) is a well-known phenomenon in fully developed turbulent square-duct flow.[1] Although relatively weak, secondary flow plays an important role in the cross-streamwise transport of heat, mass, and momentum. A complete understanding of the intimate generation mechanisms leading to the appearance of mean secondary flow would pave the way for introducing technological improvements in real-world applications and for enhancing the capabilities of turbulence models to predict SFP2nd. In the past, there have been many studies focusing on the budget of the Reynolds stress tensor and their eventual anisotropy[2,3] with the objective to explain the generation of this mean motion.

Detailed investigations of the role of the dynamics of coherent structures in low-Reynolds-number isothermal turbulent square-duct flow have been recently carried out by the present authors.[4,5] The work has highlighted the important role played by the side-walls that constrain the spanwise statistical distribution of coherent structures near the wall, i.e., quasi-streamwise vortices, low- and high-speed streaks. It has been shown that the resulting preferential locations of those structures are closely related to the pattern of the secondary flow in the isothermal cases.

In thermal square-duct turbulence under the action of gravity, which we shall discuss in this paper, the mean secondary flow will be driven not only by turbulence but also by buoyancy, and thus their coupled effects should be taken into consideration when characterizing the secondary motion. The buoyancy effects on statistics of square-duct turbulence have been studied by Ma *et al.*[6] by carrying out direct numerical simulations (DNS), with temperature difference imposed between the vertical walls of a horizontal duct,

a)Electronic mail: kawahara@me.es.osaka-u.ac.jp.

considering a wide range of Grashof numbers. They have shown that at higher Grashof numbers, a large-scale circulation motion, which is induced by buoyancy force and thus is classified as secondary flow of Prandtl's first kind (referred to as SFP1st in this paper), has a strong impact on the budget of energy also producing a strong enhancement of heat flux on the hot wall. Ma *et al.*[6] also reported that, when increasing the Grashof number, SFP2nd may experience a change to a four-vortex pattern by virtue of the thermal convection induced by the buoyancy force. In particular, they have shown the existence of a single large-scale circulation roll associated with smaller corner vortices with opposite sign of rotation. However, the physical mechanism responsible for the formation of such a peculiar four-vortex-pattern secondary flow is unknown and its eventual relationship with near-wall coherent structures and their modifications in the presence of buoyancy effects has been unclear.

In the present contribution, we extend the findings of isothermal square-duct turbulence in Refs. 4 and 5 to the case of a non-isothermal configuration. Through high fidelity numerical simulations, we determine the role played by the coherent vortical structures embedded in the flow field in producing the pattern of the mean flow of turbulence. We characterize SFP1st and SFP2nd by using the result of DNS of fully developed turbulent flow in a horizontal square duct heated from below at low Reynolds numbers.

First, we examine the dependence of the wall friction coefficient and of the Nusselt number on the bulk Richardson number that represents the ratio of buoyancy force and inertial force. Moreover, we reveal the correct scaling for the mean cross-stream velocity, rms velocity, and temperature fluctuation using a careful analysis of the mean equations supplemented by results obtained through DNS. Next, we show that the secondary flow patterns drastically change when increasing the Richardson number. On one hand, under weak buoyancy effect, we can observe the usual SFP2nd which is characterized by an eight-vortex pattern. On the other hand, when considering stronger thermal effects, the secondary flow is predominantly driven by buoyancy force leading to a large-scale circulation roll similar to the one found in a natural convection scenario concerning a two-dimensional square container[7,8] with the temperature difference imposed between horizontal walls. In-between those extreme conditions, when the intensity of the buoyancy-induced velocity is comparable with the turbulence-induced velocity, we can observe a transitional regime whose mean secondary flow presents a mixed pattern characterized by the presence of a large-scale circulation and of four small-scale vortices near the corners with a sense of rotation opposite to the large-scale circulation. We will also address the modifications of near-wall structures under the direct influence of the buoyancy-induced large circulation in order to shed some light on the nature and origin of the residual four vortex Prandtl's motions of second kind in this particular regime.

II. NUMERICAL PROCEDURE AND VALIDATION

We consider an incompressible viscous fluid flowing through an infinitely straight and horizontal square duct. As shown in Fig. 1, a Cartesian coordinate system (x, y, z) is introduced such that its origin is on the duct center line, x denotes the streamwise direction and (y, z) denote the cross-stream plane $[-h, h] \times [-h, h]$, h being the duct half width. The vertical upward direction (i.e., direction opposite to gravity) is represented by y, while x- and z-axes are parallel to the horizontal plane. All the simulations are performed imposing a constant flow rate Q. Also a constant temperature difference $\Delta T = T_h - T_c > 0$ is given between top (cold) and bottom (hot) walls (i.e., unstable temperature stratification), where T_c and T_h are the temperature of the top and bottom walls, respectively. The side walls are modeled as perfectly insulated ones.

The time evolution of the velocity vector $\boldsymbol{u} = (u, v, w)$, the pressure p, and the temperature T is described by means of the incompressible Navier–Stokes equations using the Boussinesq approximation and a transport equation for the temperature (energy equation):

$$\frac{\partial \boldsymbol{u}}{\partial t} + (\boldsymbol{u} \cdot \nabla)\boldsymbol{u} = -\frac{1}{\rho}\nabla p + \nu \nabla^2 \boldsymbol{u} + g\beta(T - T_0)\boldsymbol{e}_y, \quad (1)$$

$$\nabla \cdot \boldsymbol{u} = 0, \quad (2)$$

$$\frac{\partial T}{\partial t} + (\boldsymbol{u} \cdot \nabla)T = \kappa \nabla^2 T. \quad (3)$$

In Eq. (1), $\boldsymbol{e}_y$ is the unit vector associated to the y-direction, ρ is the constant mass density, ν is the kinematic viscosity, g (>0) is the gravity acceleration, β is the volumetric coefficient of thermal expansion, and T_0 is the reference temperature, $T_0 = (T_h + T_c)/2$. In Eq. (3), κ is the thermal diffusion coefficient. All the coefficients, ν, β, and κ, are considered to be constant. Equations (1) and (2) are advanced in time by means of a pressure correction method.[9] In particular, we use a semi-implicit scheme for the diffusive terms and a three-step low-storage Runge–Kutta method with an explicit treatment for the convective and buoyant terms:

$$\begin{aligned}\frac{\boldsymbol{u}^* - \boldsymbol{u}^{k-1}}{\Delta t} = &-2\alpha_k \frac{1}{\rho}\nabla p^{k-1} - \gamma_k[(\boldsymbol{u} \cdot \nabla)\boldsymbol{u} - g\beta(T - T_0)\boldsymbol{e}_y]^{k-1} \\ &- \zeta_k[(\boldsymbol{u} \cdot \nabla)\boldsymbol{u} - g\beta(T - T_0)\boldsymbol{e}_y]^{k-2} \\ &+ \alpha_k \nu \nabla^2(\boldsymbol{u}^* + \boldsymbol{u}^{k-1}), \end{aligned} \quad (4)$$

$$\nabla^2 \phi^k = \frac{\nabla \cdot \boldsymbol{u}^*}{2\alpha_k \Delta t}, \quad (5)$$

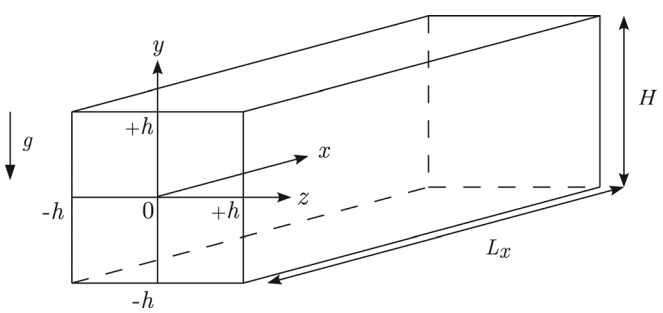

FIG. 1. Flow configuration and coordinate system.

$$\boldsymbol{u}^k = \boldsymbol{u}^* - 2\alpha_k \Delta t \nabla \phi^k, \tag{6}$$

$$p^k = p^{k-1} + \phi^k - \alpha_k \Delta t \nu \nabla^2 \phi^k, \tag{7}$$

where $k = 1, 2, 3$ is the Runge–Kutta step count ($k = 3$ being equivalent to the next time step), $\boldsymbol{u}^*$ is the predicted non-solenoidal velocity vector, and ϕ is the pseudo pressure. A set of coefficients leading to a second-order temporal accuracy for velocity and pressure[9] is $\alpha_k = \left[\frac{4}{15}, \frac{1}{15}, \frac{1}{6}\right]$, $\gamma_k = \left[\frac{8}{15}, \frac{5}{12}, \frac{3}{4}\right]$, and $\zeta_k = \left[0, -\frac{17}{60}, -\frac{5}{12}\right]$. The semi-discrete version of Eq. (3) is solved sequentially, using the most recent velocity field, viz.,

$$\frac{T^k - T^{k-1}}{\Delta t} = -\gamma_k[(\boldsymbol{u}^k \cdot \nabla)T^{k-1}] - \zeta_k[(\boldsymbol{u}^{k-1} \cdot \nabla)T^{k-2}] + \alpha_k \kappa \nabla^2 (T^k + T^{k-1}). \tag{8}$$

As far as the spatial discretization is concerned, a discrete Fourier expansion is employed to approximate the variables in the streamwise (x) direction, while Chebyshev polynomials are used in the cross-streamwise (y, z) directions. The convective terms are evaluated pseudo-spectrally with the 2/3 dealiasing technique applied in the Fourier direction. A Fourier–Galerkin treatment of the elliptic operators arising from the semi-discretized system gives rise to a set of Helmholtz and Poisson problems to be solved for each Fourier coefficient. These bidimensional problems are tackled in an efficient manner using a fast diagonalisation technique.[10] More details about the algorithm and its validation in isothermal configurations are given in Pinelli *et al.*[5]

By non-dimensionalizing governing equations (1)–(3) with full duct width H, bulk mean velocity $u_b = Q/H^2$, density ρ, and temperature difference ΔT, we have

$$\frac{\partial \tilde{\boldsymbol{u}}}{\partial \tilde{t}} + (\tilde{\boldsymbol{u}} \cdot \tilde{\nabla})\tilde{\boldsymbol{u}} = -\tilde{\nabla}\tilde{p} + \frac{1}{Re_b}\tilde{\nabla}^2 \tilde{\boldsymbol{u}} + Ri\tilde{T}\boldsymbol{e_y}, \tag{9}$$

$$\tilde{\nabla} \cdot \tilde{\boldsymbol{u}} = 0, \tag{10}$$

$$\frac{\partial \tilde{T}}{\partial \tilde{t}} + (\tilde{\boldsymbol{u}} \cdot \tilde{\nabla})\tilde{T} = \frac{1}{PrRe_b}\tilde{\nabla}^2 \tilde{T}, \tag{11}$$

where $\tilde{t} = t/(H/u_b)$, $\tilde{\nabla} = H\nabla$, $\tilde{\boldsymbol{u}} = \boldsymbol{u}/u_b$, $\tilde{p} = p/(\rho u_b^2)$, and $\tilde{t} = (T - T_0)/\Delta T$. The three non-dimensional parameters that appear in Eqs. (9)–(11) are the bulk Reynolds number, the Prandtl number, and the bulk Richardson number, defined as

$$Re_b = \frac{u_b H}{\nu}, \quad Pr = \frac{\nu}{\kappa}, \quad Ri = \frac{g\beta\Delta T H}{{u_b}^2}. \tag{12}$$

The bulk Richardson number, formed by the ratio of the buoyancy force and the inertial force, can be recast in terms of the Grashof number $Gr = g\beta\Delta T H^3/\nu^2$ and the Reynolds number Re_b as $Ri = GrRe_b^{-2}$. Another, alternative expression for the Richardson number is $Ri = (u_g/u_b)^2$, where $u_g = \sqrt{g\beta\Delta T H}$ is the velocity scale associated with buoyancy. Other non-dimensional groups that will be used hereafter are the friction Reynolds number Re_τ and the Nusselt number Nu, which are defined as $Re_\tau = u_\tau h/\nu$ and $Nu = q_w H/(\kappa \Delta T)$, where $u_\tau = \sqrt{\langle \tau_w \rangle_4/\rho}$ is the friction velocity (τ_w being the wall shear stress and $\langle\cdot\rangle_4$ being the average computed over time and over the four walls) and q_w is the local heat flux on the horizontal walls. $\langle Nu \rangle_2$ will refer to the mean Nusselt number, where $\langle\cdot\rangle_2$ is the average computed over time and over the two horizontal walls. Finally, from now on, variables with a + superscript will refer to variables normalized with u_τ and ν.

In the following, we present results from simulations performed at two Reynolds numbers: $Re_b = 3000$ and 4400. For each value of the Reynolds number, the Grashof number is changed so that the Richardson number may vary in the range $0 \le Ri \le 1.03$. At the largest value of Ri, the Boussinesq approximation can still be considered as an acceptable one in cases of square ducts with a large height and an imposed small temperature difference. For example, in the case of air flow for $u_b = 0.13$ m/s and $T_0 = 293$ K in a square duct of the full height $H = 0.5$ m, the Reynolds number is estimated as $Re_b \approx 4400$, and a small temperature difference $\Delta T = 1$ K can lead to relatively high values of $Gr \approx 2.0 \times 10^7$ and $Ri \approx 1.0$. The Prandtl number Pr is fixed to 0.7 (i.e., the working fluid is air). The values of the dimensionless parameters used for the typical numerical simulations are summarized in Table I.

All the simulations have been carried out choosing a spatial discretization verifying the following criteria: the number of Fourier modes are determined in such a way that the streamwise grid spacing is below 16.4 wall units ($\Delta x^+ < 16.4$) and the number of Chebyshev-Gauss-Lobatto collocation nodes are adjusted such that the maximum cross-streamwise grid spacing is less than 5.4 wall units (Δy^+, $\Delta z^+ < 5.4$). The CFL number is kept below 0.22 by adjusting the time step Δt. Statistical data are accumulated over a time period t_{stat} larger than $2000h/u_b$. The streamwise extension of the computational domain is taken as $L_x/h = 4\pi$, which is sufficiently long to allow for an adequate decay of the two-point velocity correlations.[3]

As already mentioned, the numerical technique used in this paper has been extensively validated by the present authors considering isothermal flows in square ducts. Particular cases at $Re_b = 4400$ and $Re_b = 7000$ have been proved to compare well with both DNS reference data of Gavrilakis[3] and with experimental data obtained from LDV measurements[11] (see the recent study of Pinelli *et al.*[5] for details). In order to validate the extension of the numerical procedure to non-isothermal conditions, we have performed numerical simulations of the same configuration as considered by Ma *et al.*[6] They have undertaken finite-difference-based DNS

TABLE I. Parameters in typical simulations.

	Re_b	Re_τ	Gr	Ri	Δx^+	$\max\{\Delta y^+, \Delta z^+\}$	Δt^+	$t_{stat}u_b/h$
(a)	3000	105.4	5.0×10^3	0.00056	10.4	3.4	0.071	2651
(b)	3000	107.0	2.0×10^5	0.022	10.5	3.47	0.074	6555
(c)	3000	111.2	5.0×10^5	0.056	10.9	3.6	0.080	2651
(d)	3000	142.2	9.0×10^6	1.00	14.0	4.6	0.13	2603
(e)	4400	149.3	5.0×10^3	0.00026	14.7	4.83	0.097	2333
(f)	4400	150.6	4.3×10^5	0.022	14.8	4.88	0.098	8482
(g)	4400	153.4	1.0×10^6	0.052	15.1	4.97	0.10	10883
(h)	4400	190.6	2.0×10^7	1.03	15.5	5.1	0.11	5687

computations in low-Reynolds-number turbulent thermal duct flow with an imposed temperature difference between the vertical walls, while assuming the horizontal walls to be perfectly insulated (a different configuration from the central subject of the present contribution). In particular, we have carried out a direct comparison for cases at $Re_b = 6200$, $Gr = 10^5$, 10^6, 10^7, and $Pr = 0.7$. Figure 2 shows a comparison of the local shear stress and the local Nusselt number on the heated vertical wall. Although small discrepancies are observed, it can be asserted that the present results show good agreement with Ma *et al.*'s predictions. A possible explanation for the slight disagreements may be given in terms of the relatively short period of time considered by Ma *et al.* for the accumulation of statistical data (their sampling time was 450 H/u_b in contrast with the present simulations that considered more than 1000 H/u_b time units). Another source of inconsistency may originate from the relatively coarser spatial resolution combined with a lower-order method used by Ma *et al.*

III. GLOBAL CHARACTERISTICS

As a first approach, in order to determine the importance of the buoyancy effects over the global behavior of both the velocity and the thermal fields, we will quantify the variations of the mean friction factor $f = 8(u_\tau/u_b)^2$ and of the mean Nusselt number $\langle Nu \rangle_2$ when increasing the value of the Richardson number. Another integral measure of the velocity field that will be considered in the analysis of Ri-dependence is the intensity of the mean secondary flow $U_\perp$ defined as $U_\perp = \left[(1/4h^2)\int_{-h}^{+h}\int_{-h}^{+h}(\bar{v}^2+\bar{w}^2)\mathrm{d}y\mathrm{d}z\right]^{1/2}$, which is useful for the characterization of buoyancy-driven flow. Hereafter $\overline{(\cdot)}$ denotes the average operator over time and streamwise direction.

In Figs. 3(a) and 3(b), the predicted values of f and $\langle Nu \rangle_2$ are given as a function of Ri for the two values of Re_b considered in the present work. Both quantities appear to be increasingly affected by buoyancy effects for values of the Richardson number $Ri \gtrsim 0.025$. If we inspect separately the friction factors for the horizontal and vertical walls, it turns out that at $Ri \gtrsim 0.025$, the friction factor for the horizontal walls is larger than that for the vertical ones (not shown here). However, the ratio of these two friction factors is observed to tend to a finite value as Ri increases, implying that the ratio is of the order of unity even for large-Ri regime. This tendency is considered to be a consequence of the geometry of a square duct of an aspect ratio of unity.

To better understand the behavior of the mean-secondary-flow intensity as a function of Ri, we introduce the decomposition $\xi(x,y,z,t) = \bar{\xi}(y,z) + \xi'(x,y,z,t)$ for all the variables, where $(\cdot)'$ represents the fluctuation about the average $\overline{(\cdot)}$. Applying the averaging operator to the dimensional momentum and temperature equations (1) and (3), one obtains the system of equations that governs the distribution of the mean variables:

$$\bar{v}\frac{\partial \bar{u}}{\partial y} + \bar{w}\frac{\partial \bar{u}}{\partial z} = -\frac{1}{\rho}\frac{\partial \bar{p}}{\partial x} - \frac{\partial \overline{u'v'}}{\partial y} - \frac{\partial \overline{u'w'}}{\partial z} + \nu\left(\frac{\partial^2 \bar{u}}{\partial y^2} + \frac{\partial^2 \bar{u}}{\partial z^2}\right), \tag{13}$$

$$\bar{v}\frac{\partial \bar{v}}{\partial y} + \bar{w}\frac{\partial \bar{v}}{\partial z} = -\frac{1}{\rho}\frac{\partial \bar{p}}{\partial y} - \frac{\partial \overline{v'^2}}{\partial y} - \frac{\partial \overline{v'w'}}{\partial z} + \nu\left(\frac{\partial^2 \bar{v}}{\partial y^2} + \frac{\partial^2 \bar{v}}{\partial z^2}\right) + g\beta(\bar{T} - T_0), \tag{14}$$

$$\bar{v}\frac{\partial \bar{w}}{\partial y} + \bar{w}\frac{\partial \bar{w}}{\partial z} = -\frac{1}{\rho}\frac{\partial \bar{p}}{\partial z} - \frac{\partial \overline{v'w'}}{\partial y} - \frac{\partial \overline{w'^2}}{\partial z} + \nu\left(\frac{\partial^2 \bar{w}}{\partial y^2} + \frac{\partial^2 \bar{w}}{\partial z^2}\right), \tag{15}$$

$$\bar{v}\frac{\partial \bar{T}}{\partial y} + \bar{w}\frac{\partial \bar{T}}{\partial z} = -\frac{\partial \overline{v'T'}}{\partial y} - \frac{\partial \overline{w'T'}}{\partial z} + \kappa\left(\frac{\partial^2 \bar{T}}{\partial y^2} + \frac{\partial^2 \bar{T}}{\partial z^2}\right). \tag{16}$$

In the case of finite Ri, when the buoyancy term may be comparable with the mean-flow convection terms, i.e., $\bar{v}(\partial\bar{v}/\partial y) \sim \bar{w}(\partial\bar{v}/\partial z) \sim \beta(\bar{T} - T_0)$, Eq. (14) provides for the balance

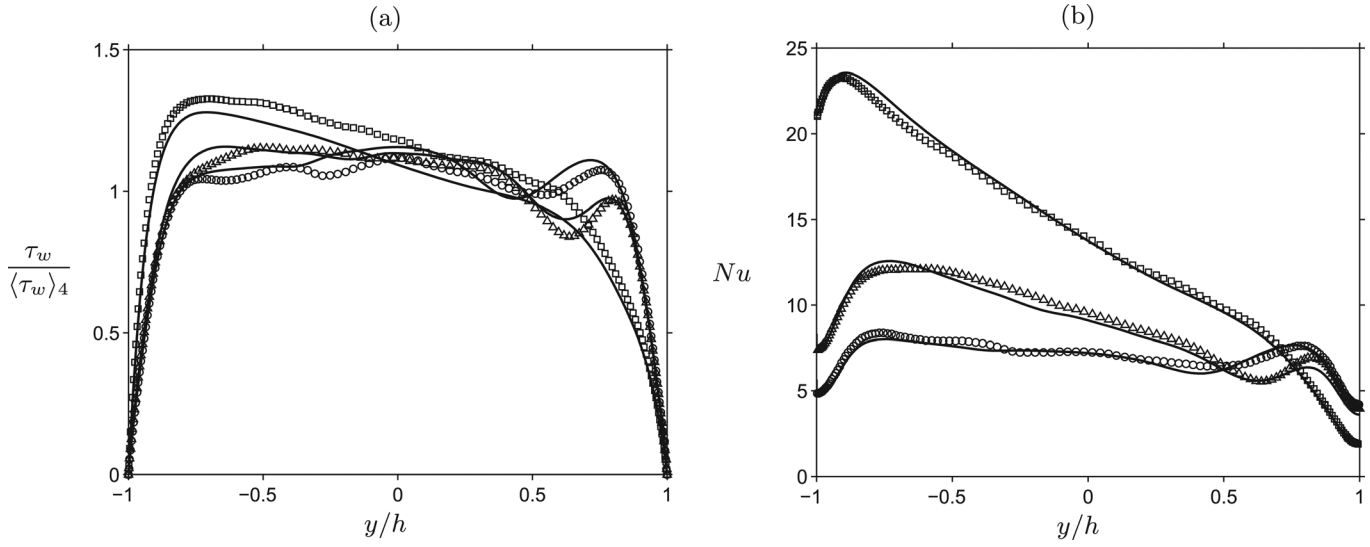

FIG. 2. The lateral variation on the heated vertical wall ($z/h = -1$) of (a) the wall shear stress τ_w and (b) the Nusselt number Nu. Solid lines represent the results from the present DNS and symbols denote Ma *et al.*'s (Ref. 6) DNS: ○, $Gr = 1.0 \times 10^5$; Δ, $Gr = 1.0 \times 10^6$; □, $Gr = 1.0 \times 10^7$.

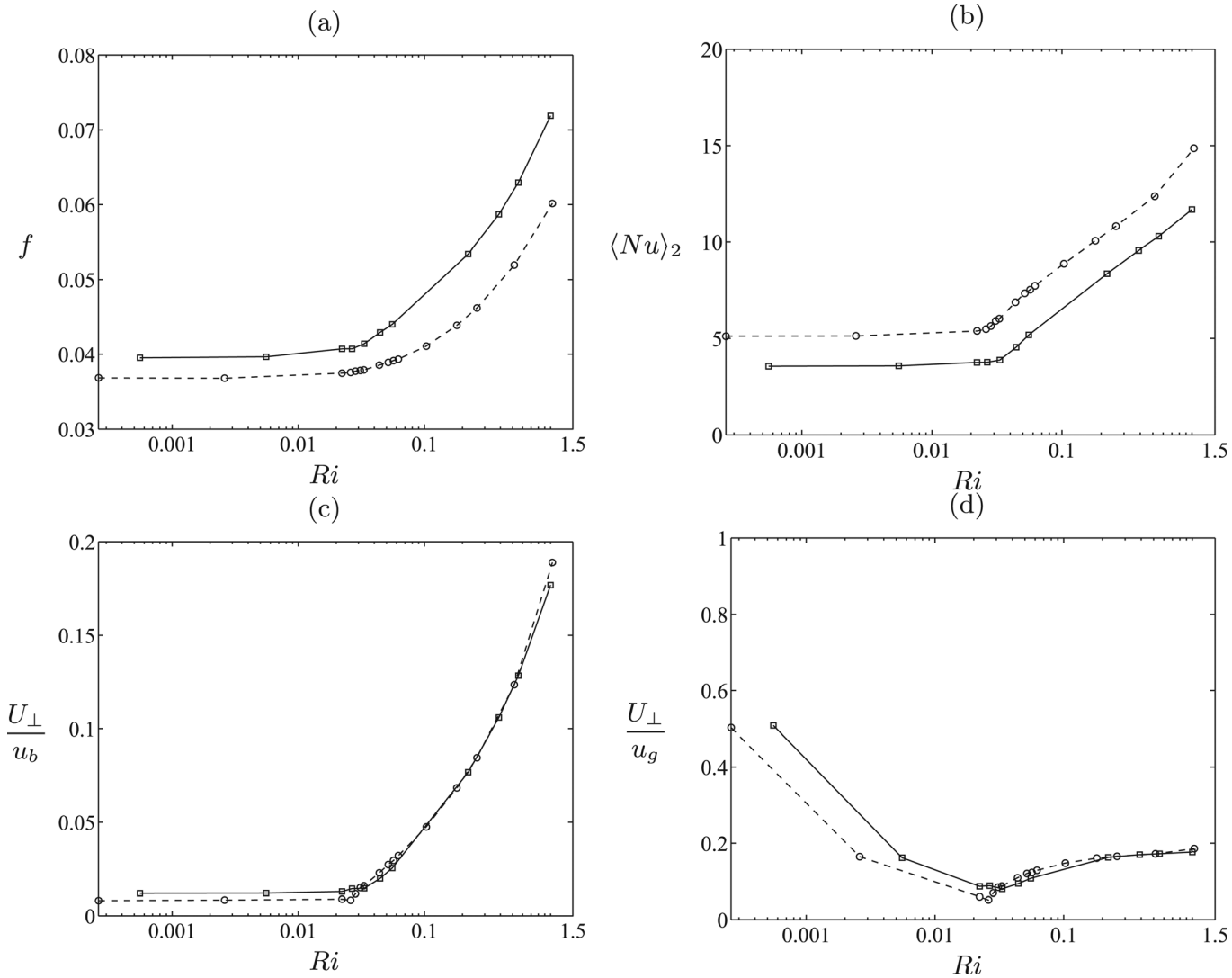

FIG. 3. The Ri-dependence of (a) the mean friction factor f and (b) the mean Nusselt number $\langle Nu\rangle_2$, and the intensity of the mean secondary flow $U_\perp$ normalized by (c) u_b and (d) $u_g = \sqrt{g\beta\Delta TH}$, respectively. —□—, $Re_b = 3000$; – – ○ – –, $Re_b = 4400$.

$$\frac{U_\perp^2}{H} \sim g\beta\Delta T, \quad \text{or equivalently } U_\perp \sim u_g = \sqrt{g\beta\Delta TH}. \tag{17}$$

In Figs. 3(c) and 3(d), $U_\perp$ is shown as a function of Ri, when normalized by u_b and u_g, respectively. The non-dimensional velocity $U_\perp/u_b$ associated with the mean secondary flow increases with Ri at $Ri \gtrsim 0.025$, thus confirming that this value of $Ri \approx 0.025$ is a threshold for buoyancy effects to come into play. Indeed, for values of $Ri \gtrsim 0.25$, the intensity of the mean secondary flow starts to scale with u_g, thus implying that the secondary flow is predominantly driven by the buoyancy force. Therefore, the mean-flow behaviors described by Fig. 3 allow for introducing three different flow regimes according to the value of Ri:

(i) $Ri \lesssim 0.025$, negligible-buoyancy regime in which buoyancy effects are negligible and therefore the mean secondary flow is solely determined by turbulence;
(ii) $0.025 \lesssim Ri \lesssim 0.25$, intermediate *equilibrium* regime in which both turbulence and buoyancy effects determine the character of the mean secondary flow;
(iii) $Ri \gtrsim 0.25$, buoyancy-dominated regime in which thermal convection determines the character of the secondary flow.

Next, we discuss the proper scalings of the rms fluctuations of both velocity and temperature fields. To this end, we consider again the set of averaged equations (13)–(16), also introducing three magnitudes to be used as a measure of the intensity of the rms fluctuations of the variables. In particular, the intensity of the cross-stream rms fluctuations will be assessed by the integral velocity value

$$U_{\mathrm{rms}\perp} = \left[(1/4h^2)\int_{-h}^{+h}\int_{-h}^{+h}\left(\overline{v'^2} + \overline{w'^2}\right)\mathrm{d}y\mathrm{d}z\right]^{1/2}. \tag{18}$$

Note that in a square duct of an aspect ratio of unity no significant difference has been observed between the cross-sectional averages of vertical and spanwise velocity fluctuations, $\left[(1/4h^2)\int_{-h}^{+h}\int_{-h}^{+h}\overline{v'^2}\mathrm{d}y\mathrm{d}z\right]^{1/2}$ and $\left[(1/4h^2)\int_{-h}^{+h}\int_{-h}^{+h}\overline{w'^2}\mathrm{d}y\mathrm{d}z\right]^{1/2}$. Analogously, to characterize the streamwise rms fluctuation the value of

$$U_{\mathrm{rms}} = \left[(1/4h^2)\int_{-h}^{+h}\int_{-h}^{+h}\overline{u'^2}\mathrm{d}y\mathrm{d}z\right]^{1/2}, \tag{19}$$

will be used. Finally, the rms fluctuation of the temperature field will be characterized by the value of

$$T_{\mathrm{rms}} = \left[(1/4h^2)\int_{-h}^{+h}\int_{-h}^{+h}\overline{T'^2}\mathrm{d}y\mathrm{d}z\right]^{1/2}. \tag{20}$$

First, we focus on the scaling of $U_{\mathrm{rms}\perp}$ by considering Eqs. (14) (or (15)). It turns out that there exist two possible balances between terms. The first one is between the mean-flow and turbulent convection terms, i.e., $\bar{v}(\partial\bar{v}/\partial y) \sim \bar{w}(\partial\bar{v}/\partial z) \sim \partial\overline{v'^2}/\partial y \sim \partial\overline{v'w'}/\partial z$ (or $\bar{v}(\partial\bar{w}/\partial y) \sim \bar{w}(\partial\bar{w}/\partial z) \sim \partial\overline{v'w'}/\partial y \sim \partial\overline{w'^2}/\partial z$), which when using the result in Eq. (17) leads to

$$u_g^2 \sim U_{\mathrm{rms}\perp}^2 \text{ or equivalently } U_{\mathrm{rms}\perp} \sim u_g. \tag{21}$$

The other possible balance concerns the equilibrium between the turbulent convection terms and the viscous ones, i.e., $\partial\overline{v'^2}/\partial y \sim \partial\overline{v'w'}/\partial z \sim \nu(\partial^2\bar{v}/\partial y^2) \sim \nu(\partial^2\bar{v}/\partial z^2)$ [or $\partial\overline{v'w'}/\partial y \sim \partial\overline{w'^2}/\partial z \sim \nu(\partial^2\bar{w}/\partial y^2) \sim \nu(\partial^2\bar{w}/\partial z^2)$], providing for the estimate,

$$U_{\mathrm{rms}\perp}^2 \sim \nu\frac{u_g}{H} \text{ or equivalently } U_{\mathrm{rms}\perp} \sim \sqrt{u_\nu u_g}, \tag{22}$$

where $u_\nu = \nu/H$ is the viscous velocity scale. Figures 4(a) and 4(b) show the reference value of the cross-streamwise rms velocity normalized with u_g and $\sqrt{u_\nu u_g}$ as a function of Ri, respectively. $U_{\mathrm{rms}\perp}/u_g$ seems to decay to zero, but $U_{\mathrm{rms}\perp}/\sqrt{u_\nu u_g}$ does not, implying that $U_{\mathrm{rms}\perp}$ could scale with $\sqrt{u_\nu u_g}$ rather than u_g.

Next, we discuss the likely scaling for the streamwise rms velocity U_{rms}. Again, the mean momentum equation in the streamwise direction [Eq. (13)] suggests two possible balances. The first one concerns the equilibrium between the mean-flow and turbulent convection terms, i.e., $\bar{v}(\partial\bar{u}/\partial y) \sim \bar{w}(\partial\bar{u}/\partial z) \sim \partial\overline{u'v'}/\partial y \sim \partial\overline{u'w'}/\partial z$, leading to

$$u_g u_b \sim U_{\mathrm{rms}}U_{\mathrm{rms}\perp} \text{ or equivalently } U_{\mathrm{rms}} \sim \frac{u_g u_b}{U_{\mathrm{rms}\perp}}. \tag{23}$$

Using relation (22), we obtain the estimate

$$U_{\mathrm{rms}} \sim u_b\sqrt{\frac{u_g}{u_\nu}}. \tag{24}$$

On the other hand, if the balance between the turbulent convection and viscous terms is supposed to take place, i.e., $\partial\overline{u'v'}/\partial y \sim \partial\overline{u'w'}/\partial z \sim \nu(\partial^2\bar{u}/\partial y^2) \sim \nu(\partial^2\bar{u}/\partial z^2)$, the following relation holds

$$U_{\mathrm{rms}}U_{\mathrm{rms}\perp} \sim u_\tau^2 \text{ , or equivalently } U_{\mathrm{rms}} \sim \frac{u_\tau^2}{\sqrt{u_\nu u_g}}, \tag{25}$$

where the last estimate has been obtained by using again the relation (22). Figures 5(a) and 5(b) show the reference values of the streamwise rms velocity as a function of Ri, normalized by $u_b\sqrt{u_g/u_\nu}$ and $u_\tau^2/\sqrt{u_\nu u_g}$, respectively. $U_{\mathrm{rms}}/(u_b\sqrt{u_g/u_\nu})$ monotonically decreases with increasing Ri, while $U_{\mathrm{rms}}/(u_\tau^2/\sqrt{u_\nu u_g})$ increases. The increase can, however, be seen to start to be saturated at larger Ri, suggesting that U_{rms} might scale according to $u_\tau^2/\sqrt{u_\nu u_g}$ rather than $u_b\sqrt{u_g/u_\nu}$.

Finally, to determine the probable scaling for the rms temperature, we consider the two possible balances offered by Eq. (16). The balance between the mean-flow and turbulent convection terms, i.e., $\bar{v}(\partial\bar{T}/\partial y) \sim \bar{w}(\partial\bar{T}/\partial z) \sim \partial\overline{v'T'}/\partial y \sim \partial\overline{w'T'}/\partial z$, yields

$$u_g\Delta T \sim U_{\mathrm{rms}\perp}T_{\mathrm{rms}} \text{ or equivalently } T_{\mathrm{rms}} \sim \Delta T\sqrt{\frac{u_g}{u_\nu}}. \tag{26}$$

From the other possible balance between the turbulent convection and the diffusive terms, i.e., $\partial\overline{v'T'}/\partial y \sim \partial\overline{w'T'}/\partial z \sim \kappa(\partial^2\bar{T}/\partial y^2) \sim \kappa(\partial^2\bar{T}/\partial z^2)$ (in this case the

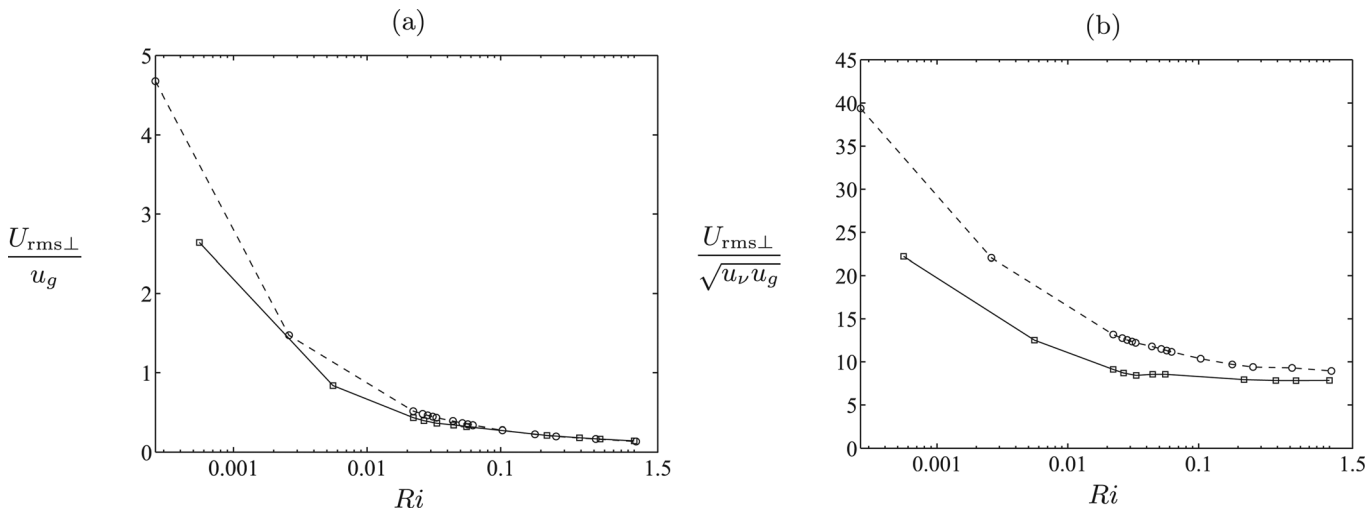

FIG. 4. The Ri-dependence of the reference cross-streamwise rms velocity $U_{\mathrm{rms}\perp}$ normalized by (a) u_g and (b) $\sqrt{u_\nu u_g}$. —□—, $Re_b = 3000$; – – ○ – –, $Re_b = 4400$.

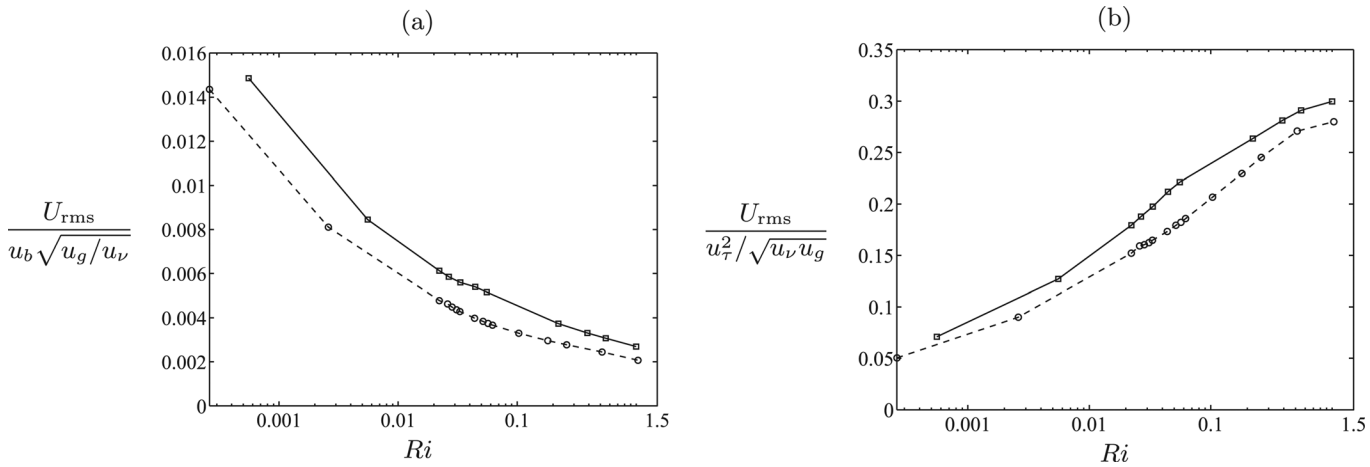

FIG. 5. The Ri-dependence of the reference streamwise rms velocity $U_{\rm rms}$ normalized by (a) $u_b\sqrt{u_g/u_\nu}$ and (b) $u_\tau^2/\sqrt{u_\nu u_g}$. — □ —, $Re_b = 3000$; – – ○ – –, $Re_b = 4400$.

two mean-flow convection terms in Eq. (16) would be in balance), we obtain

$$U_{\rm rms\perp} T_{\rm rms} \sim u_\tau T_\tau \text{ or equivalently } T_{\rm rms} \sim T_\tau \frac{u_\tau}{\sqrt{u_\nu u_g}}, \quad (27)$$

where $T_\tau = (1/u_\tau)\kappa\langle \partial T/\partial y\rangle_2$ denotes the friction temperature. The last estimates in Eqs. (26) and (27) have been obtained by use of Eq. (22). Figure 6 shows the dependence of the rms temperature on Ri when normalized by $\Delta T\sqrt{u_g/u_\nu}$ and $T_\tau u_\tau/\sqrt{u_\nu u_g}$, respectively. Although $T_{\rm rms}/(\Delta T\sqrt{u_g/u_\nu})$ monotonically decreases with increasing Ri, $T_{\rm rms}/(T_\tau u_\tau/\sqrt{u_\nu u_g})$ stays around a roughly constant value at large Ri, implying that the rms of the temperature field would scale with $T_\tau u_\tau/\sqrt{u_\nu u_g}$ rather than $\Delta T\sqrt{u_g/u_\nu}$.

The above results have indicated that the rms of the cross-streamwise velocity, the streamwise velocity, and the temperature, $U_{\rm rms\perp}$, $U_{\rm rms}$, and $T_{\rm rms}$, might scale, respectively, with $\sqrt{u_\nu u_g}$, $u_\tau^2/\sqrt{u_\nu u_g}$ and $T_\tau u_\tau/\sqrt{u_\nu u_g}$, all of which have been obtained from the balances between turbulent convection and molecular diffusion of momentum or heat.

IV. MEAN VELOCITY AND TEMPERATURE

The cross-sectional distributions of the mean streamwise and cross-streamwise velocity at the various combinations of Grashof number and Reynolds number values (as indicated in Table I) are shown in Fig. 7. At the smallest Ri (Figs. 7(a) and 7(e)), the secondary-flow vectors exhibit the usual symmetric eight-vortex patterns with respect to the wall and the corner bisectors, being typical of turbulence-driven cross-flow in the purely pressure-driven case. At slightly larger values ($Ri = 0.022$), roughly corresponding to the border between regimes (i) and (ii), the eight-vortex secondary flow is still observed, both for $Re_b = 3000$, 4400, but at the higher Reynolds number (Fig. 7(f)), the clockwise mean secondary vortices are weakened due to the buoyancy effect, so that the symmetries with respect to the wall and corner bisectors are broken.

As Ri is further increased (regime (ii)), the large-scale circulation around the duct center acts to push four pairs of counter-rotating mean secondary vortices towards the corners, so that the four clockwise vortices of the counter-

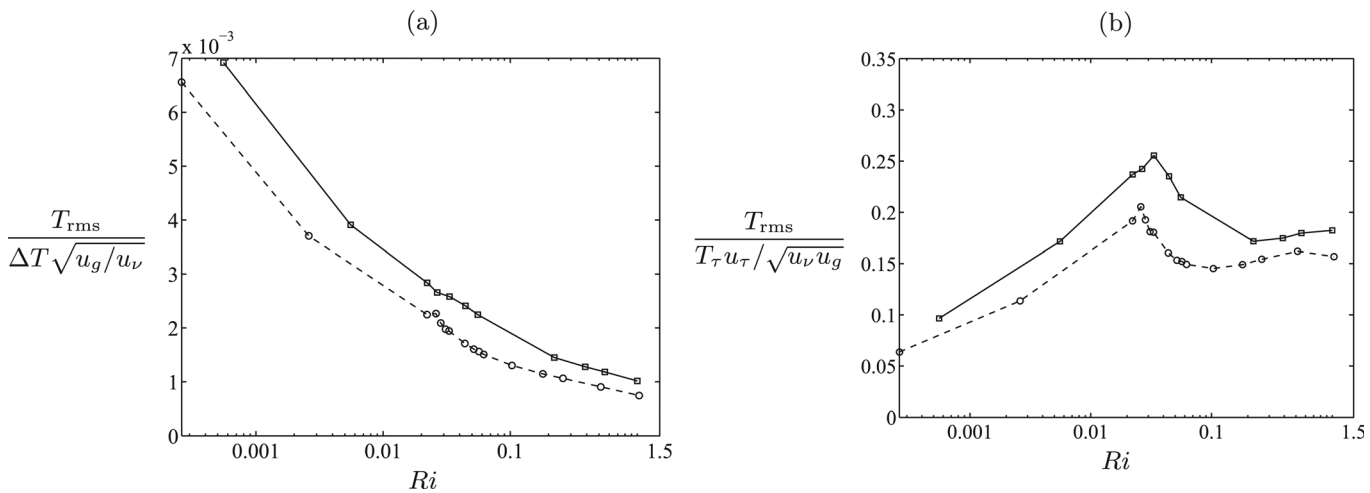

FIG. 6. The Ri-dependence of the reference rms temperature $T_{\rm rms}$ normalized by (a) $\Delta T\sqrt{u_g/u_\nu}$ and (b) $T_\tau u_\tau/\sqrt{u_\nu u_g}$. —□—, $Re_b = 3000$; – – ○ – –, $Re_b = 4400$.

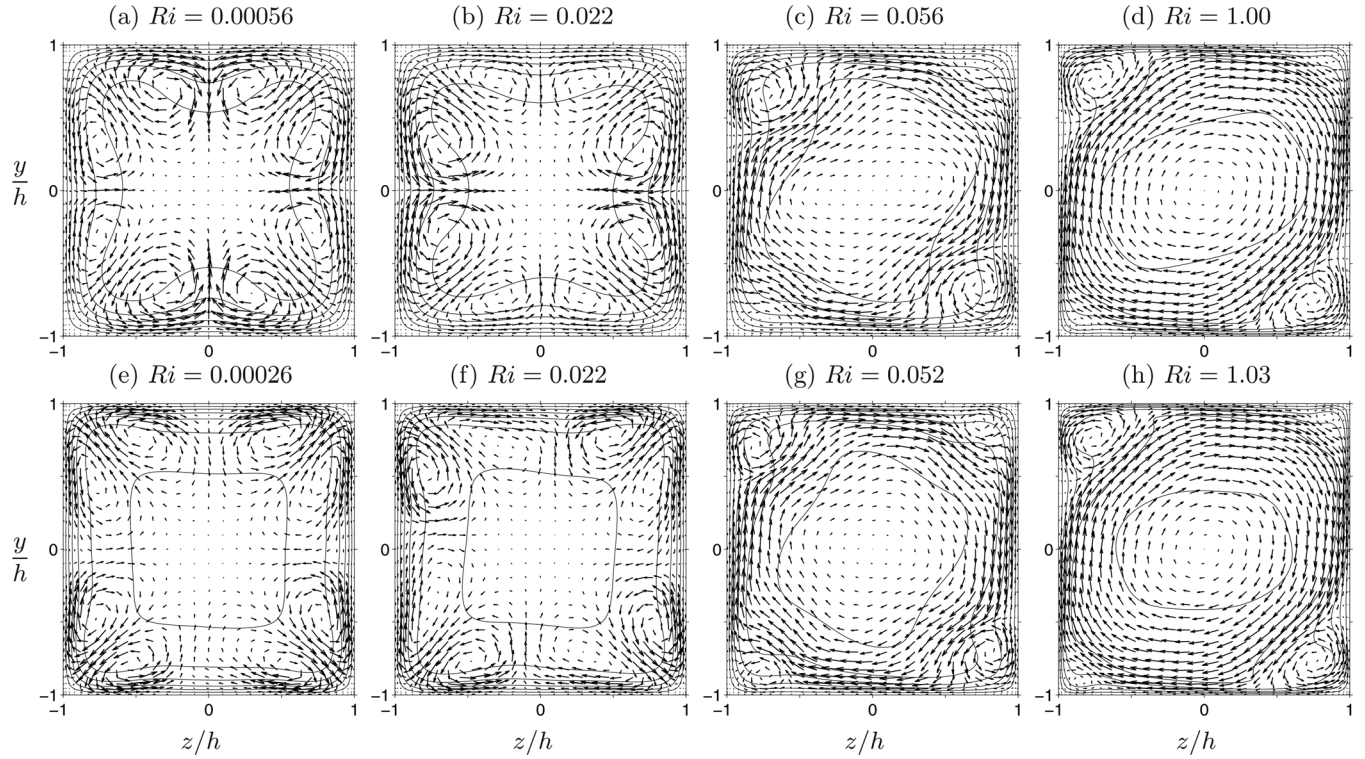

FIG. 7. Cross-sectional distributions of the mean streamwise and cross-streamwise velocity. (a)–(d) $Re_b = 3000$, (e)–(h) $Re_b = 4400$. (a) $Gr = 5.0\times 10^3$, (b) $Gr = 2.0 \times 10^5$, (c) $Gr = 5.0 \times 10^5$, (d) $Gr = 9.0 \times 10^6$, (e) $Gr = 5.0 \times 10^3$, (f) $Gr = 4.3 \times 10^5$, (g) $Gr = 1.0 \times 10^6$, and (h) $Gr = 2.0 \times 10^7$. Mean streamwise velocity is represented by iso-lines of $\bar{u}/u_b = 0.2(0.2)1.2$ and mean cross-streamwise velocity is shown by vectors. The corresponding values of the longest vectors, $\max\{\sqrt{\bar{v}^2 + \bar{w}^2}\}/u_b$, are (a) 0.024, (b) 0.028, (c) 0.029, (d) 0.145, (e) 0.020, (f) 0.021,(g) 0.027, and (h) 0.15, respectively.

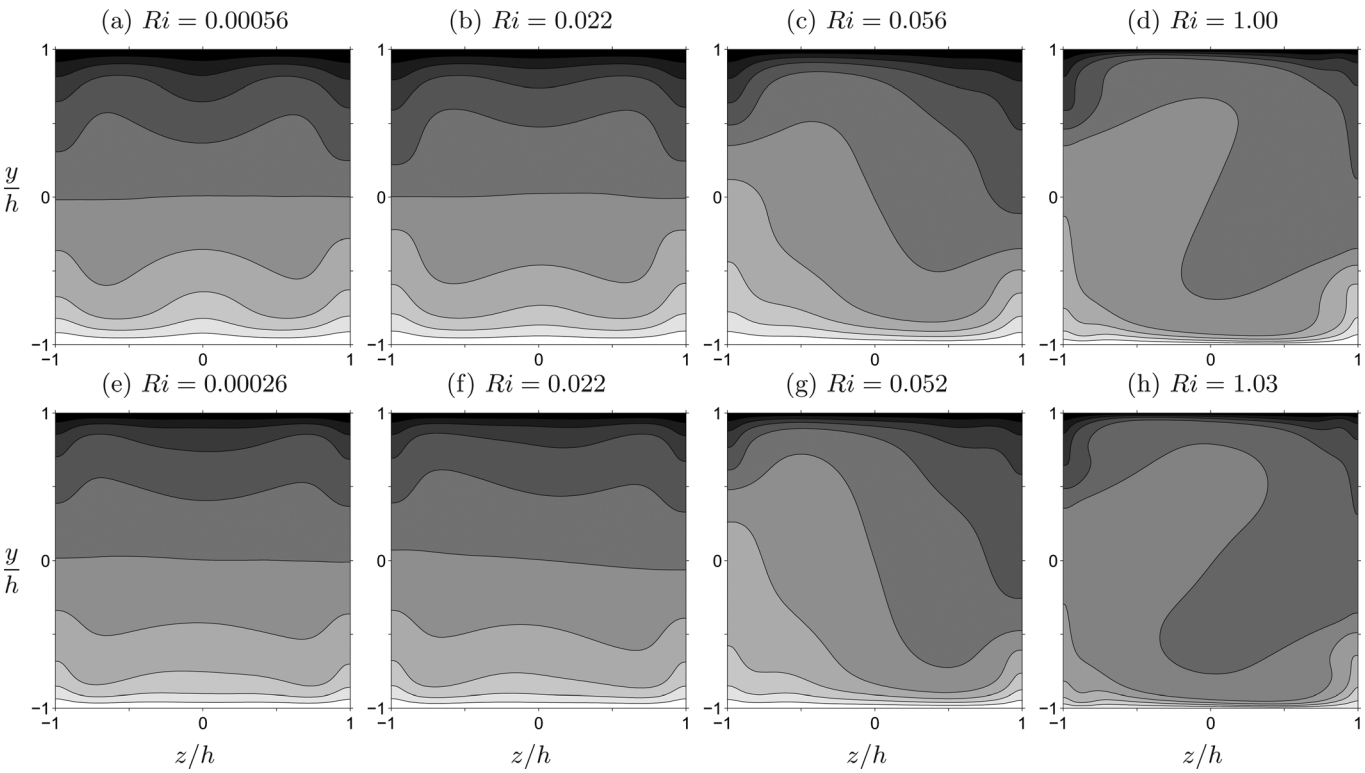

FIG. 8. Cross-sectional distribution of mean temperature represented in gray-scale with isotherms of $(\bar{T} - T_0)/\Delta T = -0.4(0.1)0.4$. (a)–(d) $Re_b = 3000$, (e)–(h) $Re_b = 4400$.

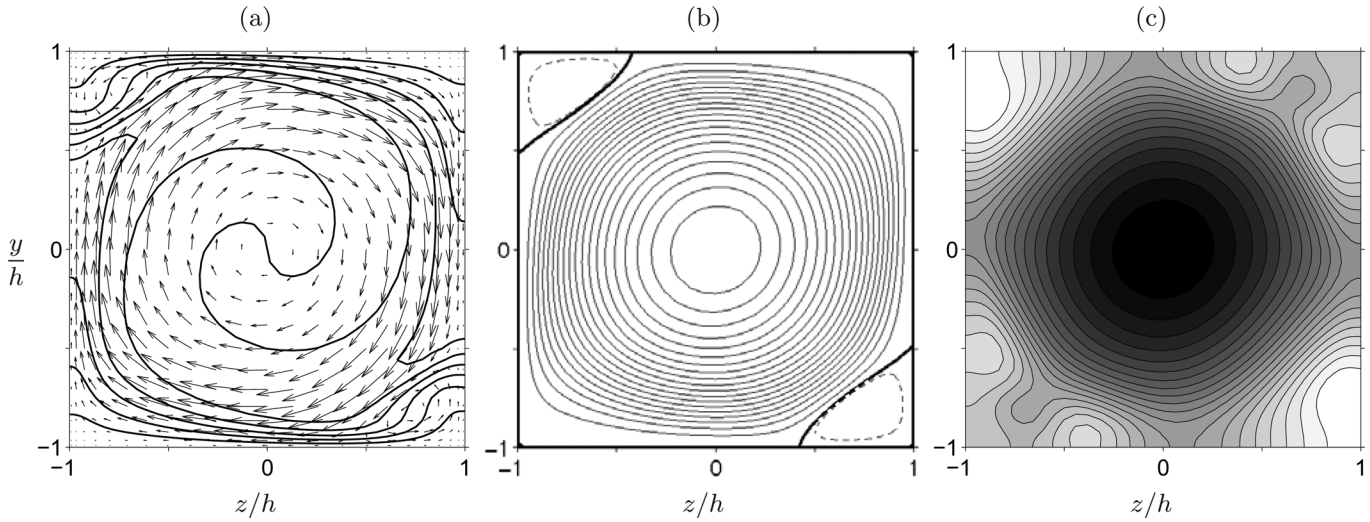

FIG. 9. The two-dimensional steady thermal convection at $Gr = 1.0 \times 10^6$. (a) The velocity and the temperature represented, respectively, by vectors and the contour lines in the interval of 0.1 ΔT. (b) The stream function ψ. The bold line represents the contour of $\psi = 0$ for the boundary. The negative contour is dashed. (c) The distribution of pressure: white, the highest pressure; and black, the lowest pressure.

rotating pairs disappear (Figs. 7(c) and 7(g)), and eventually (regime (iii)) just two counter-clockwise vortices near the upper-left and lower-right corners remain significant (Figs. 7(d) and 7(h)). Note that the symmetry of the present flow system allows the large-scale convection with the opposite-signed rotation to that in Figs. 7(c), 7(d), 7(g), and 7(h), but in this paper only the case of the clockwise circulation is shown.

The mean streamwise velocity is also shown by isolines in Fig. 7. At $Ri \lesssim 0.025$, i.e., regime (i), four pairs of the counter-rotating mean vortices with the cross-streamwise velocity scaling with u_b and so independent of Ri (see Fig. 3(c)) transport the relatively high (or low) streamwise momentum toward the duct corner (or the duct center) along the corner bisector (or the wall bisector). As a consequence, the iso-contours of the mean streamwise velocity are denser in the corner regions, implying that the wall shear is stronger near the corner than the wall bisector. At $Ri \gtrsim 0.025$ (regime (ii, iii)), on the other hand, the large-scale circulation of the velocity scale being larger for higher Ri and eventually comparable with the order of u_g (see Figs. 3(c) and 3(d)) plays a crucial role in the transfer of the high streamwise momentum toward the wall, so that the iso-contours are now much denser near the walls except for the corner regions. This momentum transfer by the large-scale circulation can enhance the wall friction with increasing Ri, as shown in Fig. 3(a).

The cross-sectional distributions of the mean temperature are shown in Fig. 8. At smaller Ri (regime (i)), the turbulence-driven four pairs of counter-rotating mean vortices induce a cross-streamwise heat transfer, and thus in Figs. 8(a), 8(b), 8(e), and 8(f), we can see the corrugation of the iso-therms caused by the mean vortices. At higher Ri (regime (ii, iii)), the buoyancy-driven large-scale circulation also plays a crucial role in the heat transfer. The roughly uniform temperature distribution around the duct center in Figs. 8(d) and 8(h) is the outcome of the large-scale heat transport and subsequent turbulence diffusion (cf. the spiral iso-therms under the action of only molecular diffusion for a comparable value of Gr in Fig. 9(a)). As discussed above for the momentum transfer, the iso-therms are much denser near the (top and bottom) walls because of the large-scale circulation, enhancing the wall heat transfer as shown in Fig. 3(b).

Although what we observed above is turbulent mixed convection, the cross-stream motion at high Ri is expected to be traced to buoyancy-driven two-dimensional flow without axial turbulent flow. Mizushima and Adachi[7] performed numerical simulations of two-dimensional steady thermal convection in a square cavity observing a single large-scale circulation and two additional corner vortices. The convection structures found by Mizushima and Adachi[7] seem to be indeed relevant to the present observations. However, their Prandtl number value $Pr = 7$ is much larger than the one considered in this paper, i.e., $Pr = 0.7$, and in their case, the temperature of the two vertical walls is fixed at the values at corresponding positions in a perfectly thermally conductive state. Sugiyama *et al.*[8] also reported the large-scale circulation and two corner vortices in their numerical simulation of two-dimensional non-Boussinesq thermal water convection in a square cavity over a wide range of the Grashof number. Therefore, we shall discuss the relevance of the mean secondary flow observed at higher Ri (or Gr) to two-dimensional thermal convection in a square container heated from below under the fully consistent conditions. The two-dimensional thermal convection is numerically examined at the same value of the Grashof number $Gr = 1.0 \times 10^6$ and the Prandtl number $Pr = 0.7$ as that for the case of $Re_b = 4400$ and $Ri = 0.052$ in Fig. 7(g) (regime (ii)). In the computation, the Fourier mode of the cross-streamwise velocity and the temperature for null streamwise wavenumber is decoupled from the other Fourier modes to represent the two-dimensional laminar flow under the same boundary conditions on the walls (i.e., adiabatic on the side-walls). Figure 9(a) shows the velocity and temperature fields of the two-dimensional laminar thermal convection. At this value of Grashof number, a steady flow

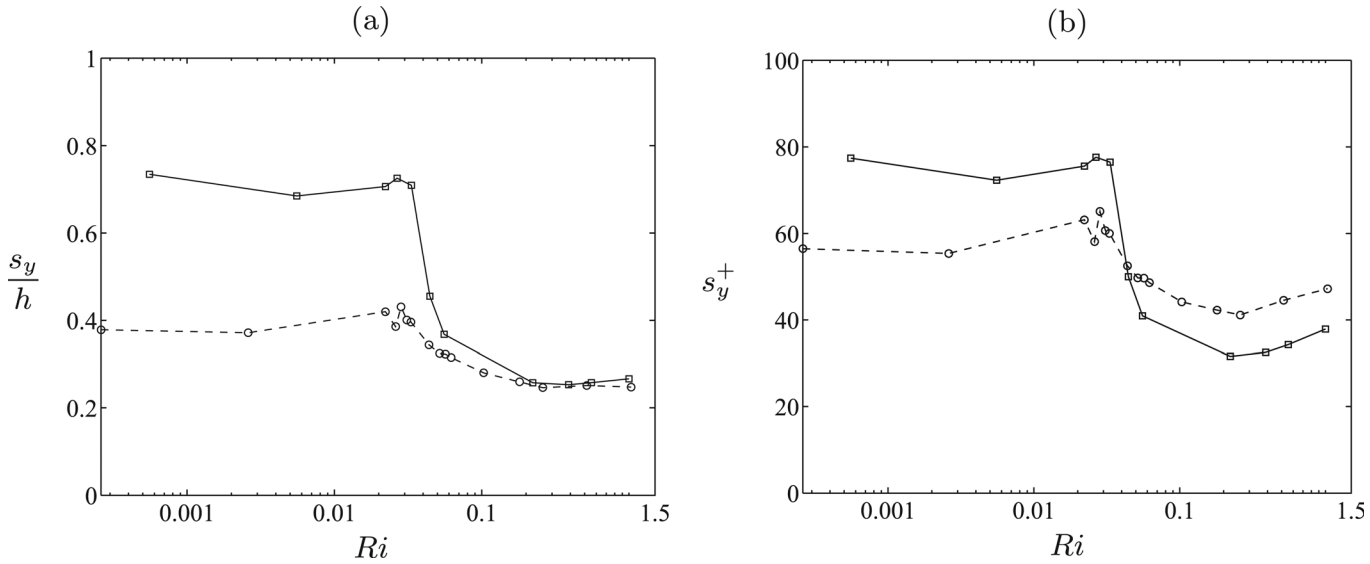

FIG. 10. The *Ri*-dependence of the position of the local minimum of the mean streamwise vorticity $\bar{\omega}_x$ for the lower-right mean secondary vortex in Fig. 7. (a) The position normalized with the duct half width. (b) The position normalized with the friction length. —□—, $Re_b = 3000$; – – ○ – –, $Re_b = 4400$.

state is observed and it is characterized in terms of the large-scale circulation and the two additional small-scale vortices in the upper-left and lower-right corner regions. Note that the thermal convection with the same sense of rotation as before is shown in the figure. The streamlines (contourlines of the streamfunction ψ) of the steady thermal convection case are shown in Fig. 9(b). The value of ψ on the walls is taken to be zero so that its positive (or negative) value may represent clockwise (or counter-clockwise) rotational motion. Significantly, negative ψ appears neither near the upper-right corner nor the lower-left corner, implying that the small-scale upper-right and lower-left mean vortices observed in Figs. 7(c) and 7(g) (regime (ii)) are turbulence-driven. On the other hand, the upper-left and lower-right mean vortices emerging in regimes (ii, iii) are considered to be buoyancy-driven, although in regime (ii), coherent structures also play a role in the formation of the mean vortices, as will be shown later.

Let us briefly discuss why only the upper-left and lower-right vortices appear in the thermal convection. Fluid close to the horizontal lower (or upper) wall are heated (or cooled), but its velocity towards the vertical left (or right) wall is relatively small, because the fluid in its vicinity cannot be directly accelerated by buoyancy in the horizontal direction. On the other hand, hot (or cold) fluid near the vertical left (or right) wall can be accelerated by buoyancy in the vertical direction, so that its velocity towards the horizontal upper (or lower) wall is larger. As a consequence, "splashing" of the high-velocity fluid on the horizontal wall would increase the pressure thereon (see Fig. 9(c)) high enough to form separation bubbles or vortices in the upper-left and lower-right corner regions.

In order to quantitatively demonstrate the behavior of the buoyancy-driven upper-left and lower-right corner vortices in Fig. 7, we show the *Ri*-dependence of the position of the extrema of the mean streamwise vorticity $\bar{\omega}_x$ in Fig. 10 (see Figs. 17(a) and 17(c) for the spatial distribution of $\bar{\omega}_x$ at $Ri = 0.052$, 1.03 and $Re = 4400$). Because the mean secondary flow in a square duct obtained from the Boussinesq approximation has π-rotational symmetry with respect to the duct center axis, we have only shown the position of the lower-right vortex. The distance s_y from the bottom wall ($y = -h$) to the position of the minimum of $\bar{\omega}_x$ for the lower-right vortex is normalized by h and friction length ν/u_τ, respectively, as shown in Figs. 10(a) and 10(b). The position of the lower-right vortex, which is also observed in the laminar convection (Fig. 9(b)), can be seen to scale with the duct width rather than the friction length in Fig. 10(a) at $Ri \gtrsim 0.25$. This is a scaling property of laminar thermal convection in which there are no multiple-scales as contrasted with turbulent flows. For $Ri \lesssim 0.25$, on the other hand, turbulence structures play a role in the formation of the mean corner vortices, and thus no clear scaling with the duct width can be educed.

V. TURBULENCE PRODUCTION AND FLUCTUATIONS

Next, we investigate velocity and temperature fluctuations. Let us first examine the production rate, per unit time, of turbulence kinetic energy $\overline{u_i'^2}/2$, that is,

$$-\overline{u_i' u_j'}\frac{\partial \overline{u_i}}{\partial x_j} + g\beta\overline{v'T'}.$$

The first contribution represents the turbulence energy production through the Reynolds stresses and the second stems from buoyancy. Figures 11 and 12 show the cross-sectional distributions of the first and second contributions to the turbulence production, respectively. At small Richardson numbers $Ri \lesssim 0.025$, the turbulence energy can be seen to be produced by the Reynolds stresses (Figs. 11(a), 11(b), 11(e), and 11(f)) in the near-wall region around the wall bisector as in the case of isothermal wall turbulence. At high Richardson numbers $Ri \gtrsim 0.025$, on the other hand, the turbulence production by the buoyancy can be seen to be comparable with that by the Reynolds stresses, and it is found that the high-

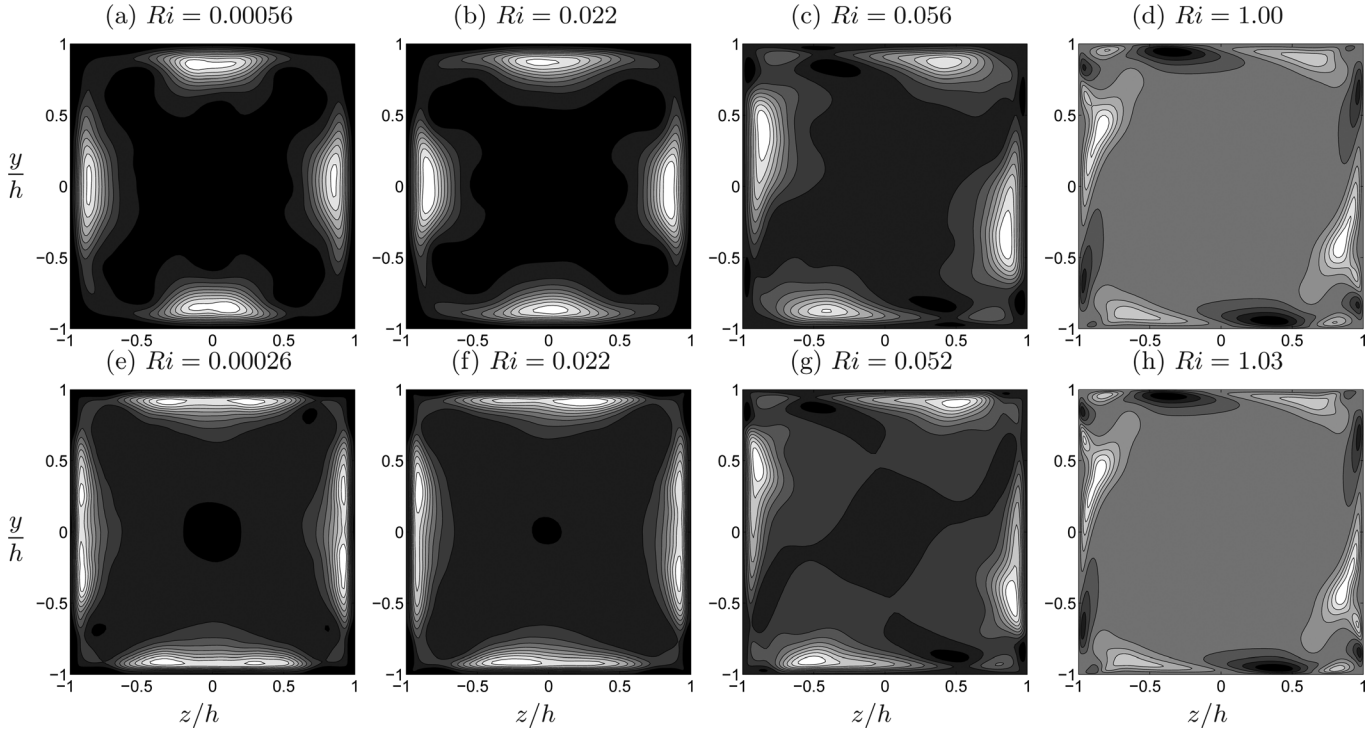

FIG. 11. Cross-sectional distribution of the turbulence energy production by the Reynolds stresses, represented in gray-scale with iso-contours (white and black shows the maximum and minimum value, respectively). The iso-contours are given by $-\overline{u_i'u_j'}\partial\overline{u_i}/\partial x_j/(u_b^3/H) \times 10^3 =$ (a) 0.36(0.76)6.44, (b) 0.31(0.79)6.63, (c) –0.65(1.24)9.27, (d) –64.7(19.7)92.9, (e) 0.07(0.92)7.43, (f) 0.02(0.98)7.86, (g) –1.3(1.5)10.7, and (h) –69.6(21.0)98.4, respectively. (a)–(d) $Re_b = 3000$, (e)-(h) $Re_b = 4400$.

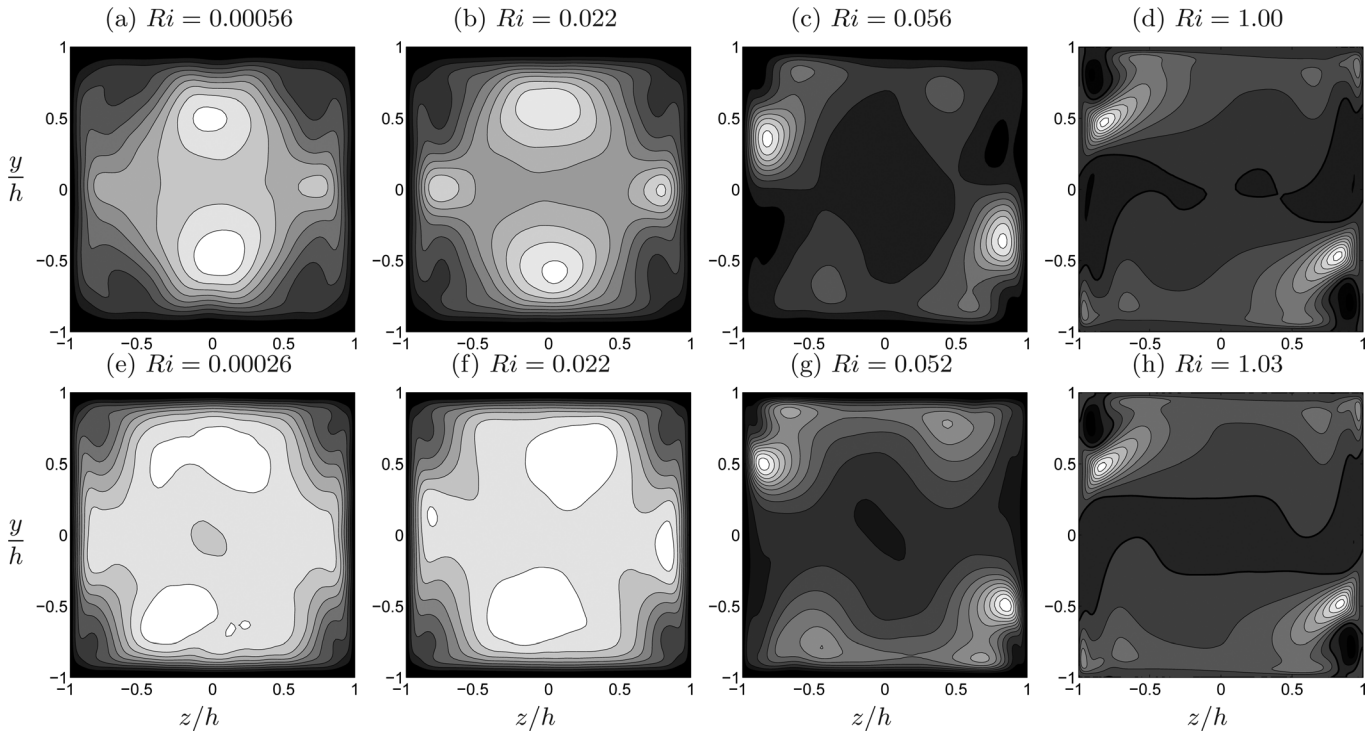

FIG. 12. Cross-sectional distribution of the turbulence energy production by buoyancy, represented in gray-scale with iso-contours (white and black shows the maximum and minimum value, respectively). The iso-contours are given by $Ri\overline{v'T'}/(u_b\Delta T) \times 10^3 =$ (a) $0.5(0.5)4.5 \times 10^{-3}$, (b) 0.02(0.02)0.18, (c) 0.09(0.09)0.81, (d) –5.5(5.9)41.7, (e) $0.2(0.2)1.8 \times 10^{-3}$, (f) 0.02(0.02)0.18, (g) 0.06(0.06)0.54, and (h) –6.9(5.5)37.1, respectively. (a)–(d) $Re_b = 3000$, (e)–(h) $Re_b = 4400$.

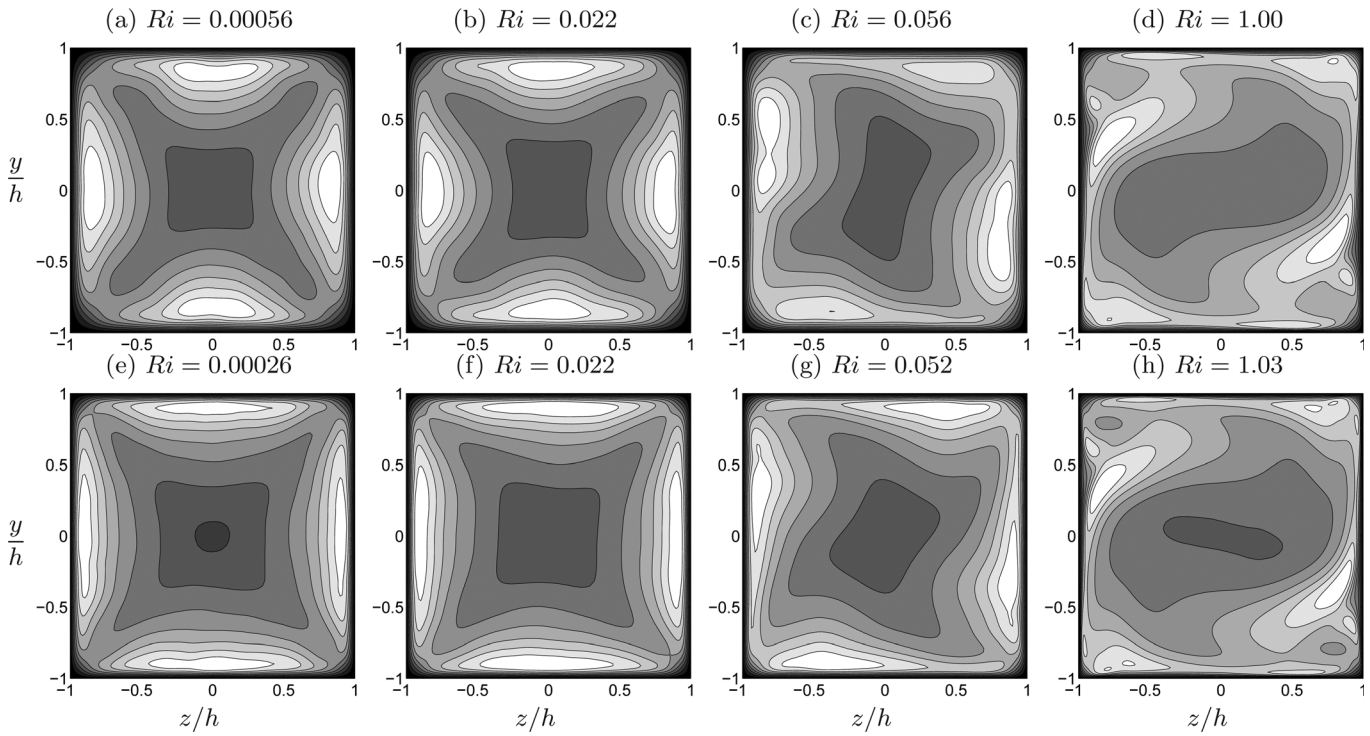

FIG. 13. Cross-sectional distribution of streamwise rms velocity $\sqrt{\overline{u'^2}}$ represented in gray-scale with iso-contours (white and black shows the maximum and minimum value, respectively). The iso-contours are given by $\sqrt{\overline{u'^2}}/u_b =$ (a) 0.066(0.066)0.594, (b) 0.067(0.067)0.603, (c) 0.066(0.066)0.594, (d) 0.063(0.063)0.567, (e) 0.065(0.065)0.585, (f) 0.064(0.064)0.576, (g) 0.061(0.061)0.549, and (h) 0.063(0.063)0.567, respectively. (a)–(d) $Re_b = 3000$, (e)–(h) $Re_b = 4400$.

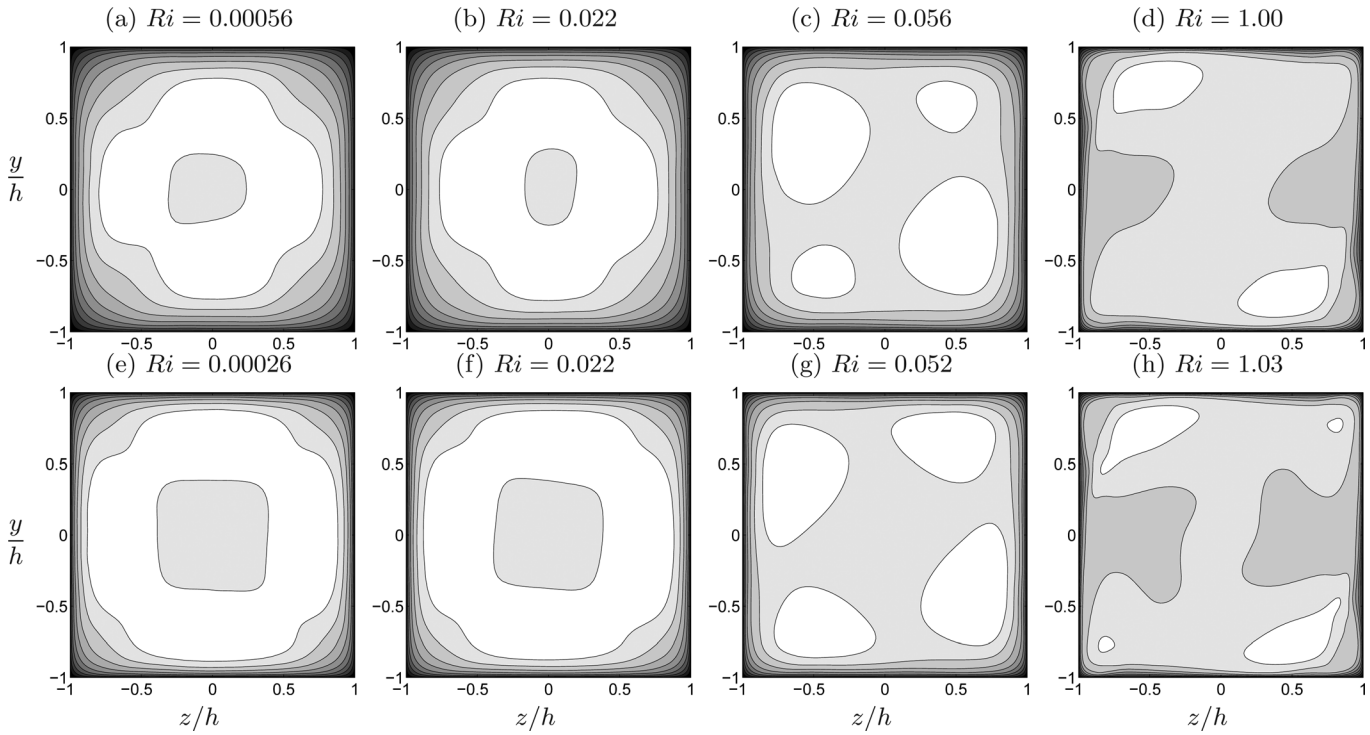

FIG. 14. Cross-sectional distribution of cross-streamwise rms velocity $\sqrt{\overline{v'^2} + \overline{w'^2}}$ represented in gray-scale with iso-contours (white and black shows the maximum and minimum value, respectively). The iso-contours are given by $\sqrt{\overline{v'^2} + \overline{w'^2}}/u_b =$ (a) 0.051(0.051)0.459, (b) 0.051(0.051)0.459, (c) 0.055(0.055)0.495, (d) 0.078(0.078)0.702, (e) 0.053(0.053)0.477, (f) 0.054(0.054)0.486, (g) 0.057(0.057)0.513, and (h) 0.077(0.077)0.693, respectively. (a)–(d) $Re_b = 3000$, (e)–(h) $Re_b = 4400$.

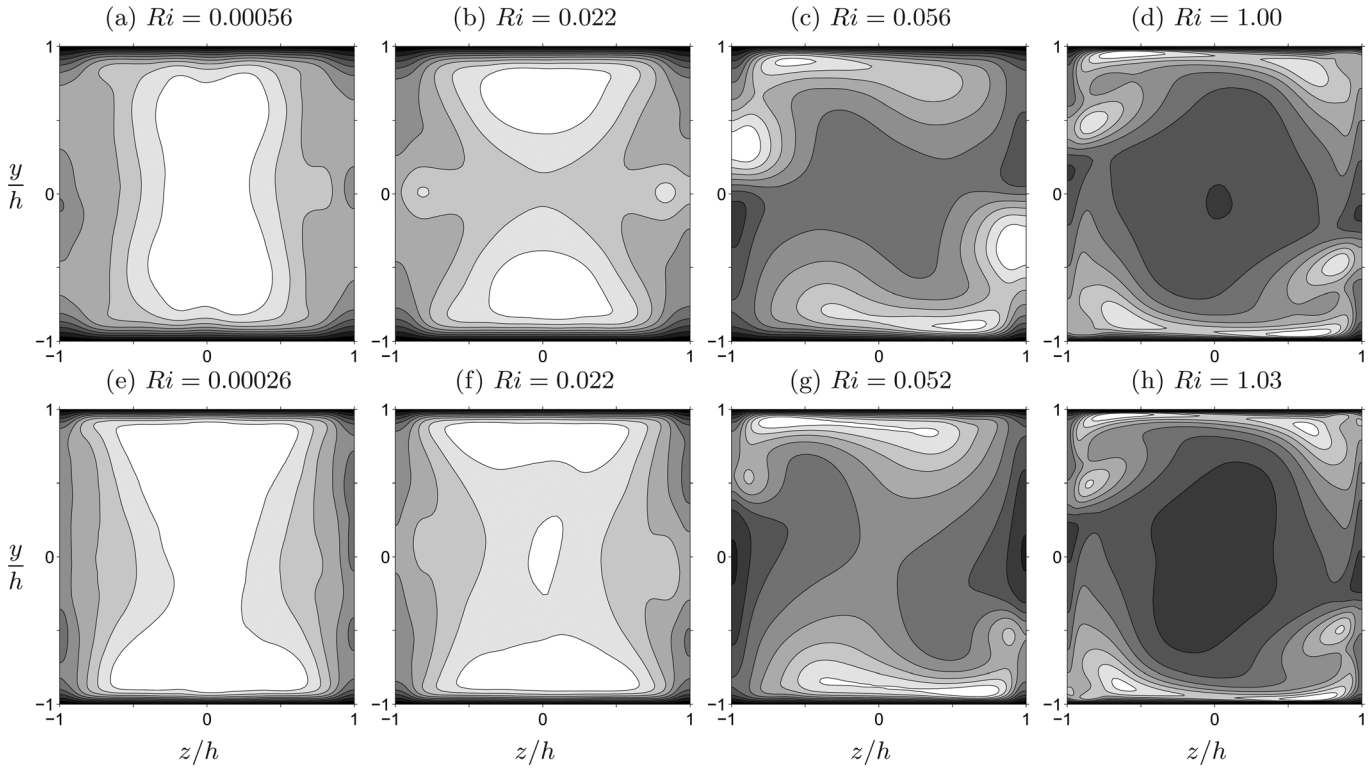

FIG. 15. Cross-sectional distribution of rms temperature $\sqrt{\overline{T'^2}}$ represented in gray-scale with iso-contours (white and black shows the maximum and minimum value, respectively). The iso-contours are given by $\sqrt{\overline{T'^2}}/\Delta T =$ (a) 0.020(0.020)0.180, (b) 0.020(0.020)0.180, (c) 0.023(0.023)0.207, (d) 0.023(0.023)0.207, (e) 0.019(0.019)0.171, (f) 0.019(0.019)0.171, (g) 0.021(0.021)0.189, and (h) 0.023(0.023)0.207, respectively. (a)–(d) $Re_b = 3000$, (e)–(h) $Re_b = 4400$.

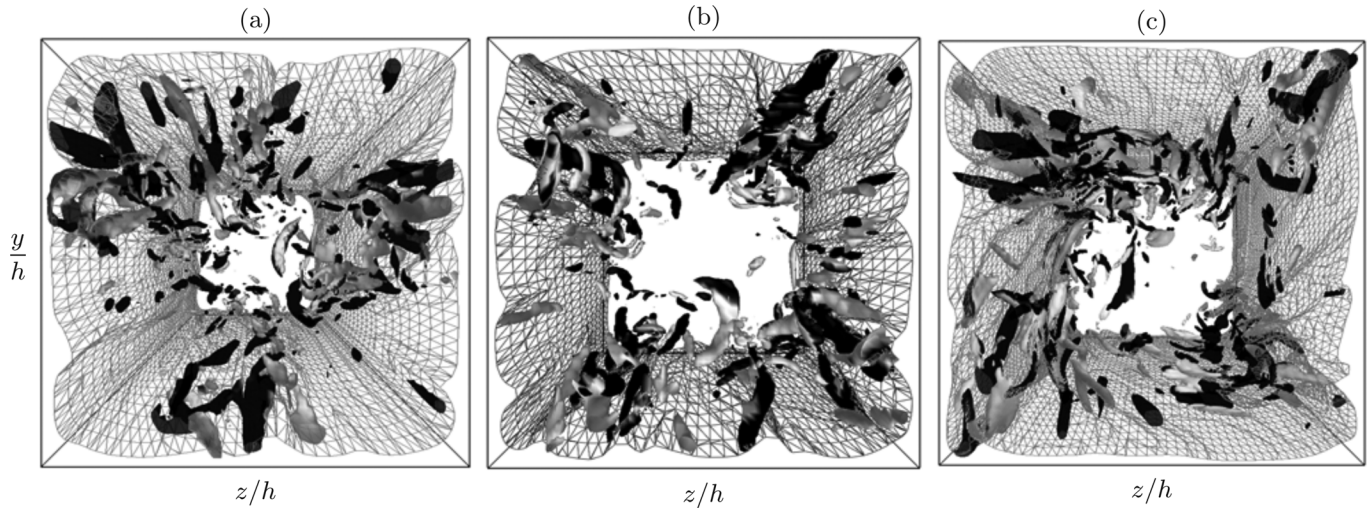

FIG. 16. The snapshots of instantaneous flow structures at $Re_b = 4400$, (a) $Ri = 0.00026$ ($Gr = 5.0 \times 10^3$, in regime (i)), (b) $Ri = 0.052$ ($Gr = 1.0 \times 10^6$, in regime (ii)), and (c) $Ri = 1.03$ ($Gr = 2.0 \times 10^7$, in regime (iii)). The streamwise velocity is shown by the gray iso-contour mesh at the level of 0.6 u_b, and the streamwise coherent vortices are shown by the iso-surfaces of the second invariant of velocity gradient tensor (Q-criterion) at the level of 0.03 u_τ^4/ν^2. The light objects are vortices with positive streamwise vorticity (the clockwise vortices) and the dark objects are vortices with negative vorticity (counter-clockwise vortices).

production regions in the two contributions overlap each other (Figs. 11, 12(c), 12(d), 12(g), and 12(h)). At $Ri \sim 1$, the highest turbulence production is observed just below (or above) the upper-left (or the lower-right) corner region corresponding to the front of the "separation bubble."

Figure 13 shows the cross-sectional distributions of the streamwise rms velocity $\sqrt{\overline{u'^2}}$. As Ri increases, the intense region of the streamwise rms velocity shifts from the wall bisector towards the corners (Figs. 13(c) and 13(g)) through the sweeping effects of the large-scale circulation. As Ri further increases (Figs. 13(d) and 13(h)), the two intense regions are separated from the side walls because of the flow detachment induced by buoyancy-driven circulation (see Fig. 9(b)). At $Ri \sim 1$, the streamwise rms velocity is relatively low around the centers of the buoyancy-driven small-scale secondary-flow vortices in the upper-left and lower-

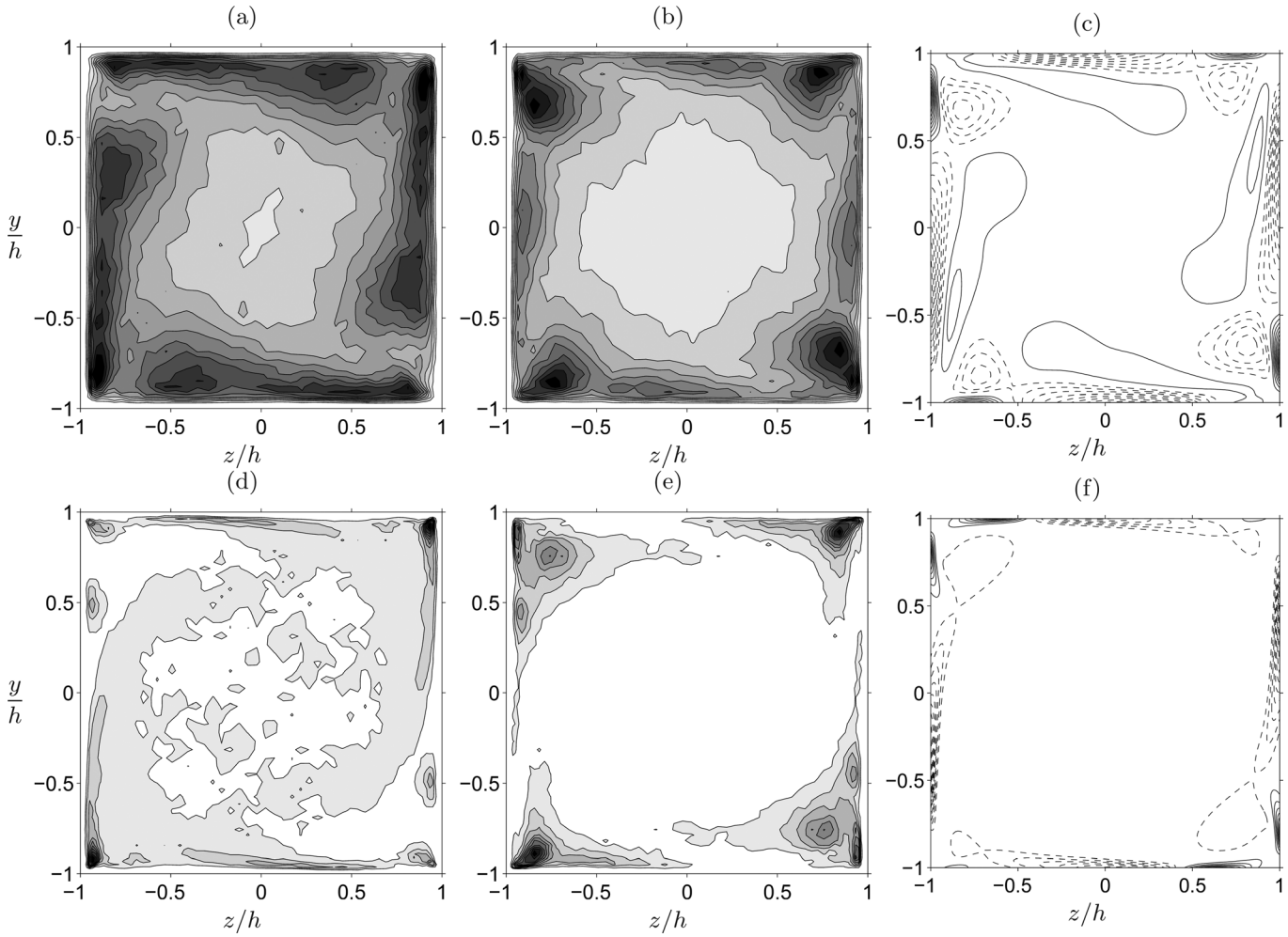

FIG. 17. Pdfs of the positions of the vortex centers (a), (d) with positive vorticity (i.e., clockwise vortices), (b), (e) with negative vorticity (i.e., counter-clockwise vortices). Pdfs are shown in gray-scale with iso-contours of increment 0.1 $P_{\max}$ (black is highest and white is null), where $P_{\max}$ is the maximum of pdf for clockwise or counter-clockwise vortices. (c, f) Mean streamwise vorticity: ——, positive vorticity (clockwise); – – – –, negative vorticity (counter-clockwise). (a)–(c) $Re_b = 4400$, $Ri = 0.052$ ($Gr = 1.0 \times 10^6$), (d)–(f) $Re_b = 4400$, $Ri = 1.03$ ($Gr = 2.0 \times 10^7$).

right corner regions, which correspond to the "separation bubbles." The cross-streamwise rms velocity $\sqrt{\overline{v'^2} + \overline{w'^2}}$ can also be seen to be relatively small in the "separation bubbles" except for their turbulent fronts (see Fig. 14), and thus the bubbles could be characterized by a roughly steady quiescent state. Actually both contributions to the turbulence energy production are small in the bubbles. On the other hand, large values of the streamwise and the cross-stream rms velocities can be observed in the upper-right and lower-left corner regions where the turbulence-driven small-scale mean secondary flow vortices exist.

Figure 15 shows the cross-sectional distributions of the rms temperature $\sqrt{\overline{T'^2}}$. In contrast to the rms velocity, large temperature fluctuations can be seen to appear in the central region of the duct at smaller Ri (Figs. 15(a), 15(b), 15(e), and 15(f)) because there is the mean temperature gradient in the vertical direction (see Figs. 8(a), 8(b), 8(e), and 8(f)), across which the turbulent fluid moves up and down. At higher Ri, on the other hand, the temperature fluctuation is very small in the central region. This is because the stirring effect of the large-scale circulation and subsequent diffusion for the temperature smooths out the mean temperature distribution around the duct center, leading to the small temperature fluctuation there.

VI. BUOYANCY EFFECTS ON FLOW STRUCTURES

Figure 16 shows snapshots of instantaneous flow fields at $Re_b = 4400$ for three values of $Ri = 0.00026$, 0.052, and 1.03, which belong to the regimes (i), (ii), and (iii), respectively. The low-velocity streaks are visualized by a gray mesh representing an iso-surface of the streamwise velocity $u = 0.6\ u_b$, and the streamwise vortices are visualized by tubular iso-surfaces of the second invariant of the velocity gradient tensor[12] at the level of $0.03(u_\tau^2/\nu)^2$, which are shaded according to the sign of the streamwise vorticity (the light objects are clockwise vortices and the dark objects are counter-clockwise vortices). The visualized streaks and vortices can be seen to be swept towards the corner by the large-scale circulation induced by the buoyancy force (cf. Figs. 16(a) and 16(b)). The shift of the intense region of the rms velocity towards the corners in Figs. 13 and 14 is attributed to this sweeping effect on these near-wall structures by the buoyancy-driven circulation. The streamwise vortices exist even at $Ri = 1.03$ and, under the action of the wall-parallel motion

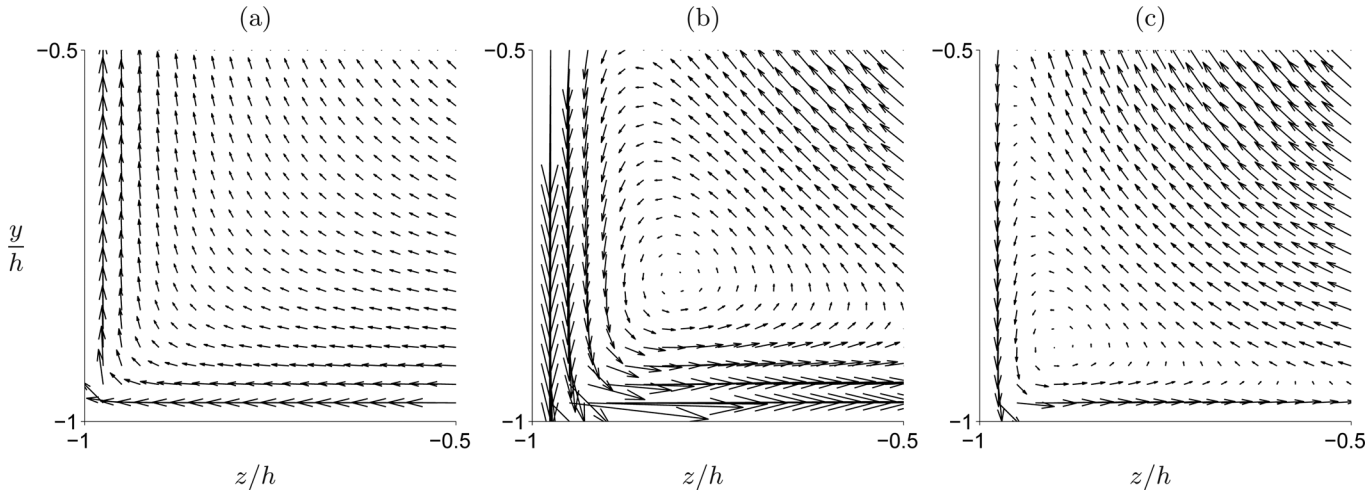

FIG. 18. Cross-sectional velocity vector fields of the vortex filament of strength γ induced by its three images expressing the two impermeable walls and by the filament of strength Γ (>0) representing the (clockwise) large-scale circulation and being fixed at $(y/h, z/h) = (0, 0)$. (a) The clockwise vortex filament subjected to the weaker circulation, Γ/γ $(\sim u_g/u_\tau) = 3.3$. (b) The counter-clockwise vortex filament subjected to the weaker circulation, Γ/γ $(\sim u_g/u_\tau) = -3.3$. (c) The counter-clockwise vortex filament subjected to the stronger circulation, Γ/γ $(\sim u_g/u_\tau) = -11.7$.

induced by the large-scale circulation, the streaks and vortices exhibit the tendency to align in the direction that is deviated from the streamwise direction in the spanwise direction.

A. Streamwise vortices

Now, we investigate the relation between the instantaneous quasi-streamwise vortices and the mean secondary flows. To quantitatively discuss it, we define the cross-sectional center of the streamwise vortices as the position of a local pressure minimum with an additional swirl condition $D < 0$, where D is the discriminant of the velocity gradient tensor in the cross-plane, i.e., $D = (\partial v/\partial y - \partial w/\partial z)^2/4 + (\partial v/\partial z)(\partial w/\partial y)$.[13] We do not need to set any thresholds to the extraction of the vortex centers in this definition. We plot the probability density functions (pdfs) of the positions of the centers of the clockwise and counter-clockwise vortices (i.e., those with positive and negative streamwise vorticity), respectively, in Figs. 17(a), 17(b), 17(d), and 17(e). The pdfs are computed by taking into account the π-rotational symmetry with respect to the duct center axis to increase the number of realizations. The result is then replicated on the upper and lower half for convenience. The corresponding mean streamwise vorticity is shown in Figs. 17(c) and 17(f).

In the case of $Re_b = 4400$ and $Ri = 0.052$, corresponding to regime (ii) in which turbulence- and buoyancy-driven secondary flow is observed, the positions of the maximum pdfs for the instantaneous counter-clockwise vortices (Fig. 17(b)) in all the corner regions can be seen to be consistent with those of the negative extrema of the mean streamwise vorticity (Fig. 17(c)). The same is not true for the instantaneous clockwise vortices (Fig. 17(a)) that do not frequently appear near the positions of the negative extrema of the streamwise vorticity in the corner regions. Except in the near regions of the corner, we cannot see remarkable differences in the pdfs for the clockwise and counter-clockwise vortices which would mostly cancel out each other. These results imply that the instantaneous streamwise coherent vortices of the opposite sense of rotation to the large-scale circulation play a role in the generation of the four mean secondary corner vortices. As will be discussed below, under the effect of the large-scale circulation as well as the geometrical constraint in the corner regions, the instantaneous vortices of the opposite sense of rotation to the circulation have a preferential location near the corner, so that the mean secondary corner vortices would appear as their statistical footprint.

Above we have observed significant differences between the patterns of the mean secondary flow in the regimes (i) and (ii) (cf. Figs. 7(a), 7(b), 7(e), 7(f), 7(c), and 7(g)). This difference would be ascribed to a marked contrast of dynamical behavior of the instantaneous vortices in the regime (ii) with that in the regime (i) in which just the geometrical constraint in the corner regions remains to accommodate the coherent vortices of both senses of rotation, leading to the appearance of the mean secondary flow exhibiting four pairs of counter-rotating vortices (see Uhlmann *et al.*[4]).

In the case of $Ri = 1.03$ allocated to the regime (iii) in which the buoyancy-driven secondary flow is dominant, the positions of the maximum pdfs for the instantaneous counter-clockwise vortices in the upper-right and lower-left corner regions (Fig. 17(e)) are still consistent with those of the weak extremum of the mean streamwise vorticity (Fig. 17(f)); however, they can be seen to shrink to the close vicinity of the corresponding corners, implying that the instantaneous vortices are confined to the smaller regions for larger Ri through the sweeping effect of the stronger large-scale circulation, as will be discussed below. Therefore, the mean secondary vortices cannot be seen clearly in the upper-right and lower-left corner regions in Figs. 7(d) and 7(h). On the other hand, the positions of the maximum pdfs in the lower-right and upper-left corner regions do not shrink, because these regions are in the "separation bubbles" that are free from the sweeping effect. In the lower-right and upper-left corner regions, there appear roughly steady buoyancy-driven secondary vortices, and thus the contribution of instantaneous vortices to the pdf therein cannot be distinguished from

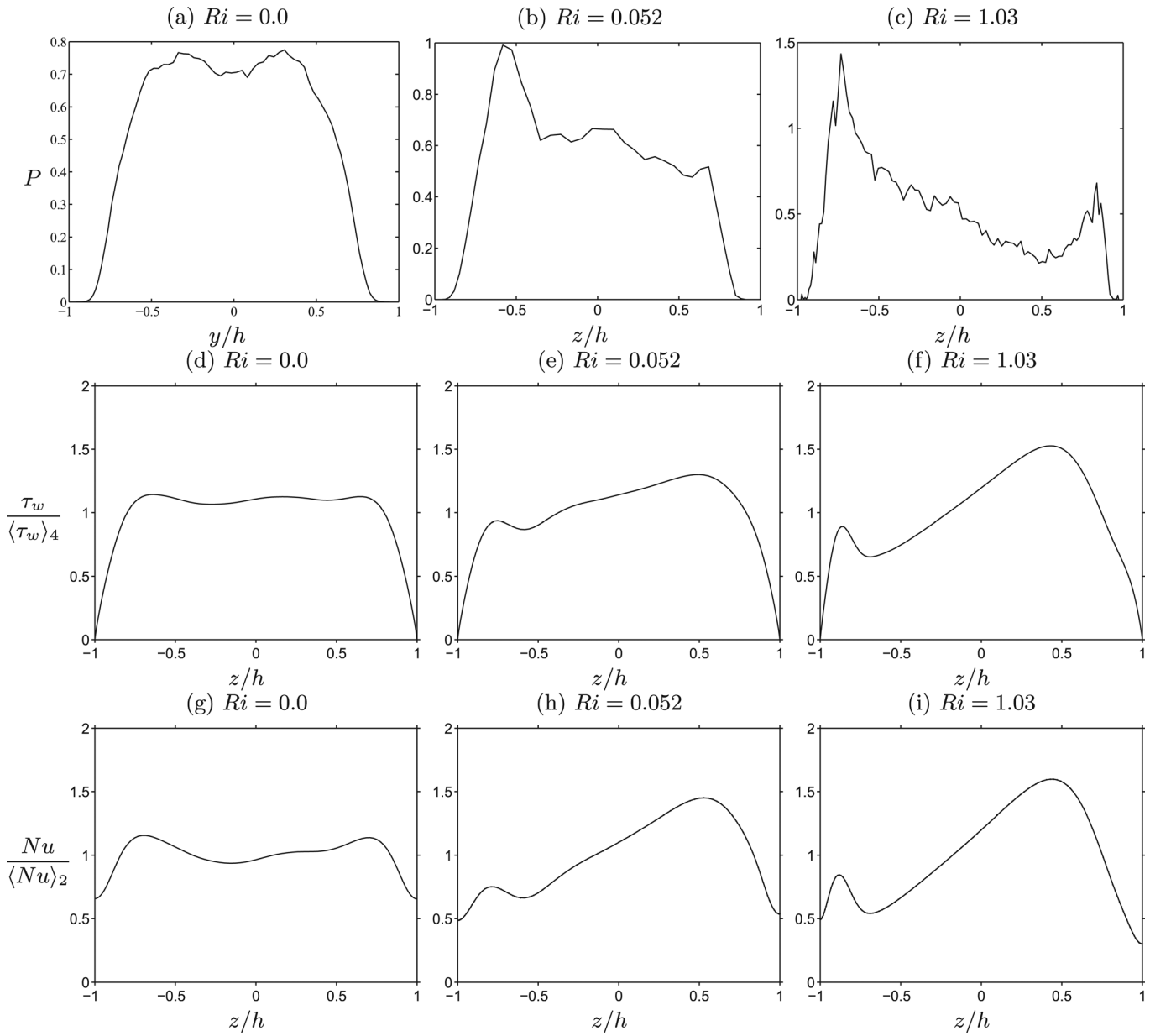

FIG. 19. Pdfs of the positions of low-velocity streaks P (a)-(c), wall shear stress (d)-(f), and Nusselt number (g)-(i) on the bottom wall $y/h = -1$ at $Re_b = 4400$. (a), (d), (g) $Ri = 0.0$; (b), (e), (h) $Ri = 0.052$; and (c), (f), (i) $Ri = 1.03$.

that of the buoyancy-driven secondary vortices. More frequent appearance of counter-clockwise vortices near the lower-right and upper-left corners (cf. Figs. 17(d) and 17(e)) is a direct consequence of the buoyancy-driven roughly steady counter-clockwise vortices.

Let us now discuss the dynamical behavior of instantaneous streamwise vortices in the near region of the corner. Since the vortical structures are elongated in the streamwise direction, and the effect of viscosity on them is not expected to be crucial, we shall consider the simplest inviscid model consisting of a streamwise vortex filament of strength γ, its three image filaments, and a fixed streamwise filament of strength $\Gamma > 0$ (clockwise rotation in Fig. 18), and its image filaments. The vortex filament of γ represents the streamwise vortex tube, and the image filaments are used to express the effects of two impermeable walls. The fixed filament is introduced to approximately take into account the swirling effects of the large-scale circulation. In the real situation at low Reynolds numbers $Re_b = 3000$ and 4400, the inner and outer length scales are not separated from each other, so that the distances from the streamwise vortex to the duct center and to the walls (or the corner), ℓ_c and ℓ_w, are of the same order. The velocity scale of the streamwise vortex in the corner region could be estimated as γ/ℓ_w, while the large-scale circulation might have the velocity of the order of Γ/ℓ_c near the corner. Therefore, the velocity ratio of the circulation to the vortex should be of the order of Γ/γ, and at the same time, it could also be estimated as u_g/u_τ, where we have supposed that the circulation and the coherent vortex have the velocity scales, u_g and u_τ, respectively.

Figure 18 shows the cross-sectional velocity vector field, for the inviscid vortex filament, induced by the inviscid

filaments representing the impermeable walls and the large-scale circulation for $\Gamma/\gamma(\sim u_g/u_\tau) = \pm 3.3$ (taken from the case of $Ri = 0.052$, $Re_b = 4400$ in Fig. 7(g)) and $\Gamma/\gamma(\sim u_g/u_\tau) = -11.7$ (taken from the case of $Ri = 1.03$, $Re_b = 4400$ in Fig. 7(h)). It can be seen in Fig. 18(b) for $\Gamma/\gamma = -3.3$ that the vector field for the counter-clockwise vortex of $\gamma < 0$ provides closed trajectories near the corner so that the vortex can stay there. The vector field for the clockwise vortex of $\gamma > 0$ in Fig. 18(a), on the other hand, does not allow closed trajectories, so that the vortex of the same sense of rotation as the circulation cannot stay near the corner. This is because in the former case, the geometrical constraint in the corner region can compensate the sweeping effect of the large-scale circulation or equivalently the cross-streamwise velocity induced by the image vortices can compensate the one induced by the circulation. For $\Gamma/\gamma = -11.7$ (Fig. 18(c)), however, the sweeping effect is much stronger, and thus it is possible only for the vortex which is close to the corner to stay there.

B. Low-velocity streaks

Next, we define the positions of low-velocity streaks near the wall as those of local minima of the wall shear on each wall. We plot the pdfs of the positions of the low-velocity streaks in isothermal and thermal ducts in Figs. 19(a)–19(c). It can be seen that the localization of the near-wall structures (streaks) in the corner region by the sweeping effects of the large-scale circulation affects the mean profile of the skin friction and the heat transfer rate on the top and bottom walls. The frequent appearance of low-velocity (Figs. 19(b) and 19(c)) and high- (or low-) temperature streaks associated with the streamwise vortices leads to the lower skin friction and heat transfer in the left (or right) corner region on the bottom (or top) wall in Figs. 19(e), 19(f), 19(h), and 19(i). The high-velocity and low- (or high-) temperature fluid is pushed towards the bottom (or top) wall by the large-scale convection, enhancing the skin friction and heat transfer in the right (or left) corner region in Figs. 19 (e), 19(f), 19(h), and 19(i).

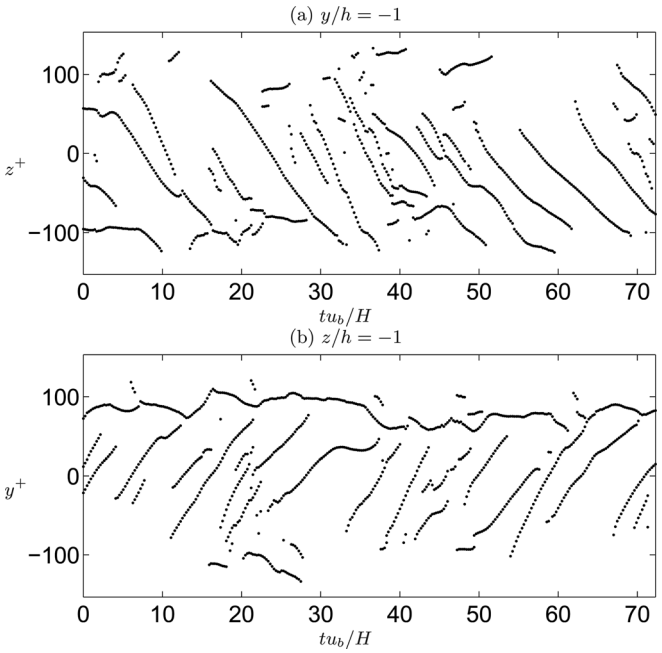

FIG. 20. Temporal evolution of the position of low-velocity streaks in the streamwise minimal turbulent flow at $Re_b = 4400$, $L_x/h = 4/9\pi$, $L_x^+ = 214.2$, $Ri = 0.052$; (a) on the bottom wall $y/h = -1$ and (b) on the vertical wall $z/h = -1$.

In order to investigate the temporal evolution of the low-velocity streaky structures, we consider a streamwise-minimal turbulent flow that can be achieved by reducing the streamwise computational domain L_x to the lowest value for sustaining turbulence.[14] Since in the minimal flow, the streamwise wavelength of the corrugated streaks coincides with L_x, their streamwise average may be used to represent the spanwise position of the streaks. We perform the DNS at $Re_b = 4400$ and $Ri = 0.052$ for $L_x/h = 4/9\pi$ ($L_x^+ = 214$) in the regime (ii), where the buoyancy-driven velocity and the turbulence-driven mean secondary velocity are comparable with each other. The minimum streamwise period to maintain turbulence in an iso-thermal square duct has been investigated systematically by Uhlmann *et al.*,[4] indicating that the minimum value is $L_x^+ \approx 190$, roughly independent of the Reynolds number.

In Fig. 20, we show the evolution of the low-velocity streaks by tracking the spanwise positions of local minima in the streamwise-averaged instantaneous wall shear profile. It can be seen on both the bottom and vertical walls that the low-velocity streaks are swept by the large-scale circulation towards the corner at $z/h = -1$ ($z^+ = -153.4$) in Fig. 20(a) and at $y/h = 1$ ($y^+ = 153.4$) in Fig. 20(b), and their spacing is roughly 100 wall units. In the near region of the corner $y/h = 1$ on the vertical wall, however, another streak remains continuously located around $y/h = 0.5$ ($y^+ \approx 80$) and it is distinct from the usual low-velocity streaks. This stationary streak is located at the front of the "separation bubble" (cf. Figs. 7(g) and 9(b)) and does not appear on the bottom wall. This result is another indication of the fundamental difference between the buoyancy-driven mean secondary vortices and the turbulence-driven ones (the upper-left and lower-right vortices, and the upper-right and lower-left ones in Figs. 7(c) and 7(g)), although the coherent structures also play a role in the formation of the upper-left and lower-right corner vortices, as discussed above.

VII. CONCLUDING REMARKS

Direct numerical simulations of fully developed turbulent flows in a horizontal square duct heated from below have been performed at bulk Reynolds numbers $Re_b = 3000$, 4400 and bulk Richardson numbers $0 \le Ri \le 1.03$. We have demonstrated the effects of buoyancy on turbulence statistics and structures, with emphasis on the characterization of the mean secondary flows of Prandtl's first and second kinds in terms of coherent vortical structures, thermal convection, and their interaction.

At small Richardson numbers $Ri \lesssim 0.025$, no visible change is observed in global properties of turbulent flow, such as mean friction factor, mean Nusselt number, and secondary-flow velocity by comparison with isothermal flow. For this range of Ri, the mean secondary flow is

characterized by four pairs of turbulence-driven counter-rotating vortices similar to those in an isothermal duct.

It is found that for $Ri \gtrsim 0.025$, the mean friction factor, the mean Nusselt number, the secondary-flow velocity, rms velocities, and temperature all increase with increasing Ri under the action of buoyancy. The cross-stream thermal convection represented by a single large-scale circulation appears to play a role in the increase of the above global quantities. The sense of the circulation depends on the initial condition, and once formed it does not alternate. Sugiyama *et al.*[8] observed reversals of the circulation sense in numerically-simulated two-dimensional chaotic thermal convection of non-Boussinesq water in a square cavity at the Rayleigh number $Ra \gtrsim 10^6$ comparable with the values of the Grashof number $Gr \gtrsim 10^7$ in the present paper. Non-reversal in the present mixed convection could be attributed to primary (streamwise) turbulent flow. The primary turbulence enhances momentum transfer, leading to the appearance of eddy viscosity. As a consequence, the effective Grashof number based on the effective viscosity (molecular plus eddy viscosity) is lower than the critical value for the reversal. It is observed that, compared to the isothermal case, the four mean secondary-flow vortices of the same sense of rotation as the circulation disappear while those of the opposite sense remain near the corners. The near-wall coherent structures are observed in the corner regions more frequently than around the wall bisector, since they are swept along the wall by the large-scale convection toward the corner. As a consequence, the near-wall intense regions of the rms velocity are shifted towards the corners. Although the coherent streamwise vortices of both senses of rotation are swept toward the corner, in the near regions of the corner, the geometrical constraint on only the vortices of the opposite sense of rotation to the circulation by impermeable walls can compensate the sweeping effect of the large-scale circulation, so that the opposite vortices stay in the corner region, leading to the generation of the four mean corner vortices of the opposite rotation.

At $Ri \gtrsim 0.25$, the buoyancy effects on the mean secondary flow become dominant, and thus only two mean corner vortices of the opposite sense of rotation remain significant since these are associated with the large-scale circulation induced by the buoyancy force as in laminar thermal convection. The large-scale circulation is observed to be stronger with increasing Ri intensifying the wall skin friction and heat transfer. At a finite value of $Ri \sim 1$, the cross-stream mean and rms velocities are found to scale, respectively, with the buoyancy-induced velocity $u_g = \sqrt{g\beta\Delta TH}$ and the mixed velocity scale $\sqrt{(\nu/H)u_g}$. Our data indicate that the scalings for the rms of streamwise velocity component and of temperature fluctuation are given, respectively, by the friction velocity and the mixed velocity scale, $u_\tau^2/\sqrt{(\nu/H)u_g}$, and by the friction velocity and temperature, and the mixed velocity scale, $T_\tau u_\tau/\sqrt{(\nu/H)u_g}$.

The scalings for the cross-stream mean and rms velocities, $U_\perp$ and $U_{\mathrm{rms}\perp}$, are rewritten in dimensionless forms as $U_\perp/u_b \sim Ri^{1/2} \sim Re_b^{-1}Gr^{1/2}$ and $U_{\mathrm{rms}\perp}/u_b \sim Re_b^{-1/2}Ri^{1/4} \sim Re_b^{-1}Gr^{1/4}$, respectively and their ratio is estimated as $U_{\mathrm{rms}\perp}/U_\perp \sim Gr^{-1/4}$. The above scaling $U_\perp/u_b \sim Re_b^{-1}Gr^{1/2}$ implies the estimate of the thermal convection Reynolds number $U_\perp H/\nu \sim Gr^{1/2}$ which coincides with that in bulk-dissipation-dominated low-Prandtl-number Rayleigh–Bénard convection.[15] The dimensionless scaling form of the streamwise rms velocity U_{rms} is given by $U_{\mathrm{rms}}/u_b \sim Re_b^{1/2} f Ri^{-1/4} \sim Re_b f\, Gr^{-1/4}$; however, in contrast to the above two expressions, we cannot show explicitly the Ri- or Gr-dependence of U_{rms} because of the existence of the friction factor f. It is also the case for the rms temperature T_{rms}, and its dimensionless scaling form is expressed as $T_{\mathrm{rms}}/\Delta T \sim Re_b^{1/2} f^{1/2} (T_\tau/\Delta T) Ri^{-1/4} \sim Re_b f^{1/2} (T_\tau/\Delta T) Gr^{-1/4}$, which includes the friction temperature T_τ in addition to f. By taking into consideration the estimation of the friction temperature $T_\tau/\Delta T \sim Re_b^{-1} Pr^{-1} \langle Nu \rangle_2 f^{-1/2}$, we obtain another expression $T_{\mathrm{rms}}/\Delta T \sim Pr^{-1} \langle Nu \rangle_2 Gr^{-1/4}$, where the Ri- or Gr-dependence of the mean Nusselt number $\langle Nu \rangle_2$ is, in turn, unknown. Figures 3(a) and 3(b) implied that f and $\langle Nu \rangle_2$ get larger with increasing Ri or Gr. Preliminary numerical inspections of f and $\langle Nu \rangle_2$ have suggested that $f \propto Gr^{1/4}$, $\langle Nu \rangle_2 \propto Gr^{1/4}$, and thus $T_\tau/\Delta T \propto Gr^{1/8}$, so that U_{rms}/u_b and $T_{\mathrm{rms}}/\Delta T$ would be finite independently of Gr. It follows from these estimates that the ratio $U_{\mathrm{rms}\perp}/U_{\mathrm{rms}}$ would increase proportionally to $Ri^{1/4}$ for fixed Re_b or equivalently to $Gr^{1/4}$.

The mean secondary motion observed in the intermediate range $Ri \approx 0.025 - 0.25$ is significantly different from the known eight-vortex secondary flow in an isothermal square duct and is a consequence of the interaction of turbulence and thermal convection. This mixed type of mean secondary flow of Prandtl's first and second kinds would be a good benchmark problem for turbulence models in the framework of Reynolds-averaging.

ACKNOWLEDGMENTS

A.S. is supported by JSPS Research Fellowship for Young Scientists. G.K. is partially supported by Grant-in-Aid for Scientific Research (B) from JSPS. The authors would like to thank Professor Sadayoshi Toh for the discussion on the formation mechanism of the flow pattern of two-dimensional steady thermal convection in a square container heated from below. The present computations were performed with the use of computing system for research at Kyushu University and supercomputing resources at Information Technology Center at the University of Tokyo.

[1] P. Bradshaw, "Turbulent secondary flows," Annu. Rev. Fluid Mech. **19**, 53 (1987).
[2] F. B. Gessner, "The origin of secondary flow in turbulent flow along a corner," J. Fluid Mech. **58**, 1 (1973).
[3] S. Gavrilakis, "Numerical simulation of low-Reynolds-number turbulent flow through a straight square duct," J. Fluid Mech. **244**, 101 (1992).
[4] M. Uhlmann, A. Pinelli, G. Kawahara, and A. Sekimoto, "Marginally turbulent flow in a square duct," J. Fluid Mech. **588**, 153 (2007).
[5] A. Pinelli, M. Uhlmann, A. Sekimoto, and G. Kawahara, "Reynolds number dependence of mean flow structure in square duct turbulence," J. Fluid Mech. **644**, 107 (2010).
[6] L.-D. Ma, Z.-Y. Li, and W.-Q. Tao, "Direct numerical simulation of turbulent flow and heat transfer in a square duct with natural convection," Heat Mass Transfer **44**, 229 (2007).
[7] J. Mizushima and T. Adachi, "Sequential transition of the thermal convection in a square cavity," J. Phys. Soc. Jpn. **66**(1), 79 (1997).
[8] K. Sugiyama, E. Calzavarini, S. Grossmann, and D. Lohse, "Flow organization in two-dimensional non-Oberbeck-Boussinesq Rayleigh-Bénard convection in water," J. Fluid Mech. **637**, 105 (2009).

[9]R. Verzicco and P. Orlandi, "A finite-difference scheme for three-dimensional incompressible flows in cylindrical coordinates," J. Comput. Phys. **123**, 402 (1996).
[10]P. Haldenwang, G. Labrosse, S. Abboudi, and M. Deville, "Chebyshev 3-d spectral and 2-d pseudo-spectral solvers for Helmholtz equation," J. Comput. Phys. **55**, 115 (1984).
[11]G. Kawahara, K. Ayukawa, J. Ochi, F. Ono, and E. Kamada, "Wall shear stress and Reynolds stresses in a low-Reynolds-number turbulent square duct flow," Trans. JSME B. **66**(641), 95 (2000) (in Japanese).
[12]A. A. Wray and J. C. R. Hunt, "Algorithms for classification of turbulent structures," in *Topological Fluid Mechanics*, edited by H. K. Mofatt and A. Tsinober (Cambridge University Press, Cambridge, 1990), pp. 95–104.
[13]S. Kida and H. Miura, "Swirl condition in low-pressure vortices," J. Phys. Soc. Jpn. **67**(7), 2166 (1998).
[14]S. Toh and T. Itano, "Interaction between a large-scale structure and near-wall structures in channel flow," J. Fluid Mech. **524**, 249 (2005).
[15]S. Grossmann and D. Lohse, "Scaling in thermal convection: A unifying theory," J. Fluid Mech. **407**, 27 (2000).